

Isotopic variation of parity violation in atomic ytterbium: method of measurements and analysis of systematic effects

D. Antypas*

Helmholtz-Institut Mainz, Mainz 55128, Germany

A.M. Fabricant

Johannes Gutenberg-Universität Mainz, Mainz 55128, Germany

J.E. Stalnaker

Department of Physics and Astronomy, Oberlin College, Oberlin, Ohio 44074, USA

K. Tsigutkin

KLA-Tencor, California, USA

V.V. Flambaum

*School of Physics, University of New South Wales, Sydney 2052, Australia and
Johannes Gutenberg-Universität Mainz, Mainz 55128, Germany*

D. Budker

Johannes Gutenberg-Universität Mainz, Mainz 55128, Germany

Helmholtz-Institut Mainz, Mainz 55128, Germany and

Department of Physics, University of California at Berkeley, California 94720-300, USA

(Dated: December 15, 2024)

We present a detailed description of experimental studies of the parity violation effect in an isotopic chain of atomic ytterbium (Yb), whose results were reported in a recent Letter [Antypas *et al.*, Nat. Phys. 15, 120 (2019) [1]]. We discuss the principle of these measurements, made on the $\text{Yb } 6s^2 \ ^1S_0 \rightarrow 5d6s \ ^3D_1$ optical transition at 408 nm, describe the experimental apparatus, and give a detailed account of our studies of systematic effects in the experiment. Our results offer the first direct observation of the isotopic variation in the atomic parity violation effect, a variation which is in agreement with the prediction of the Standard Model. These measurements are used to constrain electron-proton and electron-neutron interactions, mediated by a light Z' boson.

PACS numbers: 11.30.Er, 32.90.+a

I. INTRODUCTION

The investigation of weak-force-induced effects in atomic systems has been the focus of experiments in the last four decades (see, for example, reviews [2–4]). The first experiments were motivated by the work of Bouchiat and Bouchiat [5] which showed that weak-interaction-induced observables in atoms are enhanced and therefore are detectable in systems with large atomic number. This finding followed the earlier recognition by Zel'dovich [6] that the electron-nucleus weak interaction induces optical rotation in atomic media. Atomic physics techniques have been employed to study the parity violation (PV) at low energy. Combined with atomic structure calculations, these efforts have determined the nuclear weak charge, a quantity predicted in the Standard Model (SM), thereby testing the SM. Such tabletop experiments are complementary to studying the electroweak sector of the SM at high energies.

The first observations of atomic PV were made in bismuth (Bi) [7], thallium (Th) [8] and cesium (Cs) [9]. Accurate determinations of the PV effects were made in Bi [10], lead (Pb) [11, 12], Th [13, 14] and Cs [15, 16]. The highest measurement accuracy was achieved in Cs [15]. Combined with precise atomic-structure calculations [17], the Cs experiment resulted in a determination of the nuclear weak charge at the level of 0.5%. This result is the most-precise-to-date low-energy test of the SM.

Atomic PV experiments can additionally be platforms to study nuclear physics as well as physics beyond the SM. Measurements of nuclear-spin-dependent contributions to the PV effect probe the nuclear anapole moment [18–20], which has only been observed to date in the Cs experiment [15]. Determining an anapole provides information about the so-far poorly understood weak meson-nucleon couplings that characterize the hadronic weak interactions, as formulated in the model of Desplanques, Donoghue, and Hollstein [21]. Measurements of PV across a chain of isotopes of the same element, first proposed in [22], have the potential to probe the variation of the neutron distribution in the nucleus, and

* dantypas@uni-mainz.de

to test nuclear models [23, 24]. In addition, atomic PV studies can be used to search for light bosons beyond the SM that mediate parity-violating interactions between the electron and nucleons [25].

A number of PV experiments are currently underway, that make use of neutral atoms, as well as atomic ions and molecules. Of these, an experiment in Fr [26] is aiming to determine the nuclear weak charge, as well as to measure the anapole moment of Fr nuclei. Another project with Fr, currently at a preliminary stage [27], also aims to measure the weak charge and anapole. An experiment using a single trapped Ra^+ ion [28], aims to determine the nuclear weak charge in several different isotopes. An ongoing experiment in Cs [29] is primarily focused on a cross-check measurement of the Cs anapole moment. Improved measurements of PV are underway in Dy [30], in which a previous experiment yielded an effect consistent with zero [31]. Finally, an effort with BaF [32, 33] has recently demonstrated adequate sensitivity to make an accurate determination of the anapole moment of the Ba nucleus.

We recently reported on measurements of PV in the $6s^2\ ^1S_0 \rightarrow 5d6s\ ^3D_1$ optical transition at 408 nm in a chain of four nuclear-spin-zero Yb isotopes [1]. That work provided an observation of the isotopic variation of the PV effect, and was part of a program that focuses on nuclear spin-dependent PV, neutron skins, as well as on searching for light bosons beyond SM. These results built upon an earlier observation of the Yb PV effect [34, 35]. The previous measurement confirmed the large size of the effect, which was first estimated in [36], with more elaborate calculations following up [37–39]. Here we present in detail the method utilized for these isotopic-chain measurements, discuss the experimental apparatus, and provide an analysis of systematic effects.

II. EXPERIMENTAL METHOD

To study PV in Yb, we make use of the $6s^2\ ^1S_0 \rightarrow 5d6s\ ^3D_1$ optical transition at 408 nm (fig. 1). The experimental principle was described in [35]. A small electric-dipole ($E1$) transition amplitude arises between the 1S_0 and 3D_1 states, mainly due to weak-interaction-induced mixing between the 3D_1 and 1P_1 states. The application of a quasi-static electric field creates additional (Stark) mixing between the same states [40], and introduces a Stark-induced $E1$ amplitude for the 408 nm transition. A static magnetic field is also applied to the atoms to split the Zeeman sublevels of the excited 3D_1 state. With appropriate choice of geometry for the applied static and optical fields, the Stark and PV amplitudes interfere [41]. The sign of this interference in the 408 nm excitation rate can be changed by making field reversals, allowing extraction of the P-odd part of this rate from the larger P-even background. For the geometry of fields in the present experiment (fig. 2), the Stark-PV interference is proportional to the following pseudo-scalar

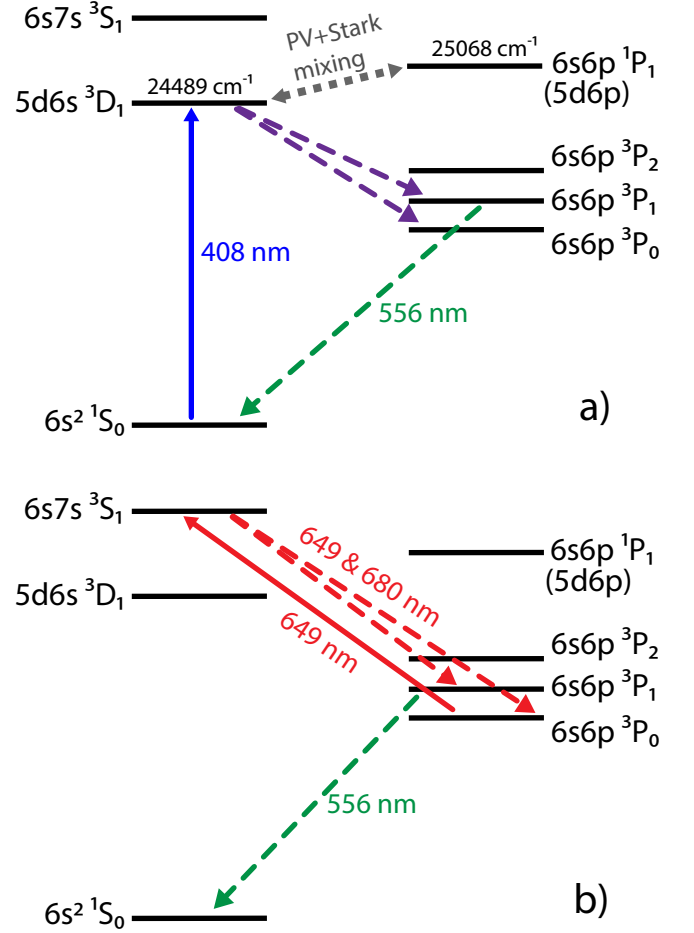


FIG. 1. (Color online) a) Energy levels relevant for the Yb PV experiment with the 408 nm transition. The PV-effect arises primarily due to weak-interaction-induced mixing of the 3D_1 and 1P_1 levels. About 2/3 of atoms undergoing the 408 nm transition decay to the 3P_0 metastable state. b) Detection of the population in the 3P_0 state via fluorescence induced by further excitation to 3S_1 .

rotational invariant [41, 42]:

$$(\vec{\mathcal{E}} \cdot \vec{B}) \cdot ([\vec{E} \times \vec{\mathcal{E}}] \cdot \vec{B}), \quad (1)$$

where \vec{E} , $\vec{\mathcal{E}}$ and \vec{B} are, respectively, the quasi-static electric, optical and magnetic fields applied to the atoms. The Stark and PV amplitudes for the $m=0 \rightarrow m'$ component of the $^1S_0 \rightarrow ^3D_1$ transition are given by [35]:

$$A_{m'}^{Stark} = i\beta(-1)^{m'}(\vec{E} \times \vec{\mathcal{E}})_{-m'}, \quad (2)$$

$$A_{m'}^{PV} = i\zeta(-1)^{m'}\vec{\mathcal{E}}_{-m'}, \quad (3)$$

where $\beta = 2.24(12) \cdot 10^{-8} e a_0 / (\text{V/cm})$ is the vector polarizability of the transition, determined in [43, 44], and ζ is the $E1$ transition moment arising primarily from the PV-mixing of the 3D_1 and 1P_1 states. The parameter ζ is

proportional to the nuclear weak charge. The element V_q is the q -component of the vector \vec{V} in the spherical basis. The results presented here come from measurements on the $m = 0 \rightarrow m' = 0$ transition component, whereas the previous experiment [34, 35] utilized all three magnetic sublevels of the 408 nm transition to determine the PV-effect.

The effects of a magnetic-dipole ($M1$) transition between the 1S_0 and 3D_1 states, whose amplitude is ≈ 1000 times greater than that of the PV-amplitude, are suppressed in this experiment. The experimental geometry is such that the $M1$ and Stark amplitudes are out of phase and do not interfere. Additional suppression occurs because the $^1S_0 \rightarrow ^3D_1$ excitation is done with a standing-wave optical field (see Appendix A).

In the absence of non-reversing fields and field misalignments, the magnetic field is along the z -axis, $\vec{B} = B_z \hat{z}$, and the electric field along the x -axis, $\vec{E} = (E_{dc} + E_0 \cos \omega t) \hat{x}$. This field consists of a component oscillating at frequency ω ($\omega/2\pi = 19.9$ Hz) as well as a dc-term. The ac-component, of typical amplitude 1 kV/cm, is primarily responsible for the required Stark-induced mixing between 3D_1 and 1P_1 states. The change of the ac-field direction is the primary parity reversal in the experiment. The dc term E_{dc} (≈ 6 V/cm) is used to optimize detection conditions for the Stark-PV interference. The optical field is linearly polarized and propagates along x : $\vec{\mathcal{E}} = \mathcal{E}(\sin \theta \hat{y} + \cos \theta \hat{z})$. Under these conditions, the excitation rate for the $m = 0 \rightarrow m'$ transition component has the form:

$$R_{m'} \propto |A_{m'}^{Stark} + A_{m'}^{PV}|^2 = R_{m'}^{[0]} + R_{m'}^{[1]} \cos \omega t + R_{m'}^{[2]} \cos 2\omega t. \quad (4)$$

This rate consists of a dc term of amplitude $R_{m'}^{[0]}$, and components oscillating at frequencies ω and 2ω with respective amplitudes $R_{m'}^{[1]}$ and $R_{m'}^{[2]}$. For the $0 \rightarrow 0$ transition these terms are as follows:

$$R_0^{[0]} = 2\mathcal{E}^2 \beta^2 E_0^2 \sin^2 \theta + 4\mathcal{E}^2 \beta^2 E_{dc}^2 \sin^2 \theta + 8\mathcal{E}^2 \beta E_{dc} \zeta \cos \theta \sin \theta, \quad (5)$$

$$R_0^{[1]} = 8\mathcal{E}^2 \beta E_0 \zeta \cos \theta \sin \theta + 8\mathcal{E}^2 \beta^2 E_0 E_{dc} \sin^2 \theta, \quad (6)$$

$$R_0^{[2]} = 2\mathcal{E}^2 \beta^2 E_0^2 \sin^2 \theta. \quad (7)$$

Only terms independent of or linear in the weak-interaction parameter ζ are retained in (4), (6) and (7). Phase-sensitive detection at the frequencies ω and 2ω provides the amplitudes $R_0^{[1]}$ and $R_0^{[2]}$. Their ratio is related to the ratio of the PV- and Stark-induced transition moments:

$$r_0 \equiv \frac{R_0^{[1]}}{R_0^{[2]}} = \frac{4E_{dc}}{E_0} + \frac{4\zeta}{\beta E_0} \cot \theta. \quad (8)$$

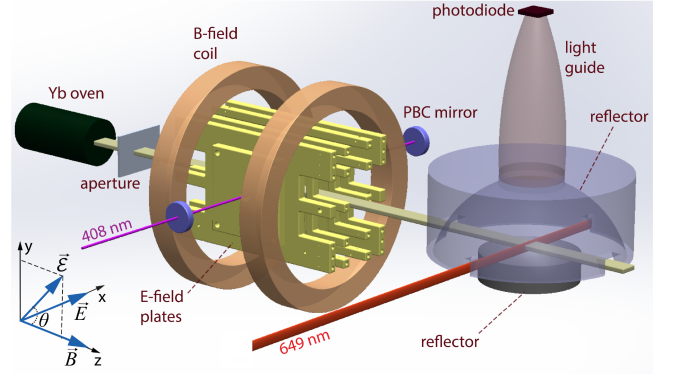


FIG. 2. (Color online) Schematic of the Yb atomic-beam apparatus. The Yb atoms effuse from the oven into the interaction region, where they are excited by 408 nm light in the presence of applied electric and magnetic fields. The atoms that are excited are detected in the downstream detection region via excitation from the metastable state at 649 nm.

Observation of the change in r_0 under the second parity reversal, i.e. a $\pm\pi/2$ rotation of the light polarization plane, yields the ratio ζ/β . In addition to the E - and θ - reversals (parity reversals), the magnetic field \vec{B} as well as the polarity of E_{dc} are also reversed, in order to study and minimize systematic contributions, not explicitly shown in (8).

Misalignments of the applied fields, non-reversing field components, as well as imperfections in the optical polarization alter the ideal situation discussed above, and result in additional contributions to the transition rate (4) and to the ratio (8). The applied electric field and magnetic fields are most generally given by:

$$\vec{E} = (E_{dc} + E_0 \cos \omega t) \hat{x} + (e_y + e_y^r \cos \omega t) \hat{y} + (e_z + e_z^r \cos \omega t) \hat{z}, \quad (9)$$

$$\vec{B} = (b_x + f_B b_x^r) \hat{x} + (b_y + f_B b_y^r) \hat{y} + (b_z + f_B B_z) \hat{z}. \quad (10)$$

The component v_i denotes the stray (non-reversing) component of the vector \vec{V} along the i -axis, and v_i^r the reversing \vec{V} component along the same axis. A B-field flip parameter $f_B = \pm 1$ is introduced in (10). All the field components containing the term f_B reverse with the main magnetic field. Allowing for an ellipticity in the nominally linearly polarized optical field, $\vec{\mathcal{E}}$ becomes:

$$\vec{\mathcal{E}} = \mathcal{E}(\sin \theta \hat{y} + \cos \theta e^{i\phi} \hat{z}). \quad (11)$$

As discussed in [35], a rotation operation has to be applied to the fields of (9), (10) and (11) so that the rotated \vec{B} is along z . The transition rate (4), as well as the harmonics amplitudes $R_0^{[1]}$ and $R_0^{[2]}$, acquire then a large number of terms. A series expansion in the field imperfections and ζ yields a harmonics ratio $r_0(\theta, f_B)$, in which, in addition to the PV-related term ζ/β , terms that transform in the same way as ζ/β under the θ -reversal, are also present. The full expression for $r_0(\theta, f_B)$ in the

presence of apparatus imperfections is given in Appendix A. A simplified expression, that includes the only significantly contributing PV-mimicking term, is the following:

$$r_0(\theta, f_B) = \frac{4E_{dc}}{E_0} + \left[\frac{4\zeta}{\beta E_0} + \frac{4(b_x + f_B b_x^r)e_y}{f_B B_z E_0} \right] \cot \theta \cos \phi. \quad (12)$$

There are four different values of $r_0(\theta, f_B)$, corresponding to the two possible values of the polarization angle ($\theta \approx \pm\pi/4$) and magnetic field direction ($f_B = \pm 1$), and four different ways to combine these values. These combinations, labeled K_i ($i=1,2,3,4$), are computed using the full expression for $r_0(\theta, f_B)$ (see Appendix A) as follows:

$$\begin{pmatrix} K_1 \\ K_2 \\ K_3 \\ K_4 \end{pmatrix} = \begin{pmatrix} +1 & -1 & +1 & -1 \\ -1 & -1 & +1 & +1 \\ -1 & +1 & +1 & -1 \\ +1 & +1 & +1 & +1 \end{pmatrix} \cdot \begin{pmatrix} r_0(\theta_+, +1) \\ r_0(\theta_-, +1) \\ r_0(\theta_+, -1) \\ r_0(\theta_-, -1) \end{pmatrix}. \quad (13)$$

The values of K_i are given in Table I. One of these (K_1) yields the ratio ζ/β ; the others provide important information about parasitic fields and overall measurement consistency. Some of the K_i values are expressed in terms of the polarization parameter p , defined as:

$$p = \cot \theta_+ \cos \phi_+ - \cot \theta_- \cos \phi_-, \quad (14)$$

with $p \approx 2$ in the experiment. The angles ϕ_{\pm} are the ellipticity-related parameters corresponding to the angles θ_{\pm} . Examination of the terms in K_1 shows that a precision determination of ζ/β requires, aside from accurate knowledge of E_0 , a measurement of the false-PV contribution $e_y b_x^r/B_z$ as well as a measurement of the parameter p . Methods to make these measurements are discussed in section IV.

TABLE I. The four combinations of harmonics ratio $r_0(\theta, f_B)$ values, corresponding to the two orientations of the polarization angle ($\theta_{\pm} \approx \pm\pi/4$) and magnetic field ($f_B = \pm 1$). The angles ϕ_{\pm} are the small optical field ellipticity-related parameters for the polarization states with angles θ_{\pm} , respectively.

Combination	Value
K_1	$\left(\frac{8\zeta}{\beta E_0} + \frac{8b_x^r e_y}{B_z E_0} \right) p$
K_2	$\frac{16b_x e_z}{B_z E_0} - \frac{32b_y \zeta}{\beta B_z E_0}$
K_3	$-\frac{8b_x e_y}{\beta B_z E_0} p$
K_4	$\frac{16E_{dc}}{E_0} - \frac{16b_x^r e_z}{B_z E_0} + \frac{32b_y \zeta}{\beta B_z E_0}$

III. APPARATUS

The PV isotopic comparison experiment was carried out with a newly built atomic-beam apparatus which has

increased statistical sensitivity and better ability to study and control systematics, compared to that of [34, 35].

A schematic of the in-vacuum setup is shown in fig. 2. An Yb atomic beam is produced with an oven heated to ≈ 550 °C. Atoms exiting the oven nozzle travel a distance of ≈ 28 cm to reach the interaction region, with a mean longitudinal velocity of ≈ 290 m/sec and a transverse velocity spread of ≈ 8 m/s (Full Width at Half Maximum-FWHM). In the interaction region, the atoms intercept the 408 nm standing-wave optical field, tuned to excite the $^1S_0 \rightarrow ^3D_1$ transition. This light circulates in a power-build-up cavity (PBC), which has a finesse of ≈ 550 and is used to enhance the light power available to excite atoms, but also to suppress the effects of the $M1$ -Stark interference. The circulating power is measured by recording the light transmitted through the PBC, and it is actively stabilized, to a level of ≈ 55 W. This stabilization results in negligible contribution of intracavity power noise to noise in detection of the excitation rate on the 408 nm transition. The waist ($1/e^2$ intensity radius) of the optical beam in the interaction region is $w_0 \approx 310$ μm , corresponding to an intensity of ≈ 18 kW/cm 2 . The intracavity power level is a compromise between the need for large 408 nm excitation rate and unwanted distortion in the transition lineshape, which becomes significant at large intracavity intensities [44, 45]. A representative lineshape for the 408 nm transition is shown in fig. 3.

The required electric field is applied to the atoms with a system of gold-coated electrodes. This system consists of two main plates, approximately 10×10 cm 2 , spaced by 5.5045(20) cm. A set of eight surrounding electrodes is employed to increase field uniformity as well as to apply auxiliary field components in either the y- or z- direction, for systematics studies. Six high-voltage amplifiers and a system of voltage dividers are used to bias the main plates and surrounding electrodes. Simulations of the electric field with COMSOL[®] yield a value for the primary field of $[1 - 2.7(3) \cdot 10^{-4}] \cdot V/d$, where V is the potential difference between the plates, and d is the plate spacing. The non-uniformity of the field within the 1.5 cm wide interaction region (whose diameter is 0.6 mm) is lower than 0.1%. The magnetic field in the interaction region of 93 G is applied with a pair of round in-vacuum coils, which have nearly Helmholtz geometry. Additional sets of coils are used to cancel the residual field in the interaction region (to within 20 mG), as well as to apply additional field components for studies and control of systematics.

Detection of the 408 nm excitations in the interaction region is done downstream in the path of the atoms using an efficient detection scheme described in detail in [35, 47]. The fraction of atoms ($\approx 65\%$) that decayed to the 3P_0 metastable state after undergoing the 408 nm transition, are further excited with ≈ 120 μW of 649 nm light to the 3S_1 state (see fig. 1), in the region of an optimized light collector (fig. 2). The light collector directs the induced fluorescence at 556, 649 and 680

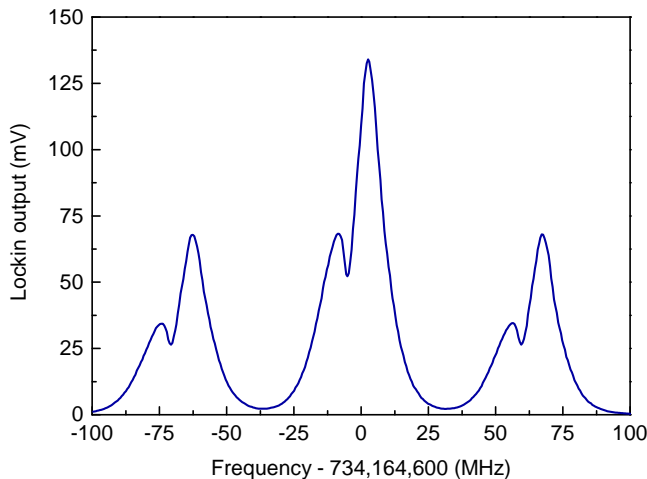


FIG. 3. (Color online) Spectrum of the $^{174}\text{Yb } ^1\text{S}_0 \rightarrow ^3\text{D}_1$ transition lineshape. The spectrum is recorded by scanning the 408 nm laser frequency around the center of the resonance. The applied 93 G magnetic field splits the magnetic sublevels of the $^3\text{D}_1$ level, resulting in fully-resolved transition components $m = 0 \rightarrow m = 0, \pm 1$. The width (FWHM) of the resonance profile is 18 MHz. The profile distortion is due to the effects of the off-resonant ac-Stark effect in the presence of the intense 408 nm standing-wave field. This spectral profile distortion has been studied extensively in [44, 45], and can be removed if needed using methods demonstrated in [46].

nm to a light-pipe which guides light out of the vacuum chamber and onto the surface of a large-area photodiode, whose photocurrent is amplified with a low-noise transimpedance amplifier. This amplifier has a 1 G Ω transimpedance and ≈ 1.1 kHz bandwidth. The overall detection efficiency of the 408 nm transitions is an estimated 25% [48].

The 408 nm laser system is a frequency-doubled Ti:Sapphire laser (M² SolStiS+ECD-X) outputting ≈ 1 W of near-UV light. The laser frequency is stabilized to an internal reference cavity, with a resulting linewidth of less than 100 kHz. The short-term stability of the system is sufficiently good so that we use the internal cavity as the short-term frequency reference. The PBC is stabilized to this reference through frequency-modulation spectroscopy; the PBC length is modulated at 29 kHz using a piezo-transducer onto which one of the cavity mirrors is mounted, and the demodulated PBC transmission is applied back to the piezo with an electronic filter. During an experiment, the laser frequency is locked to the peak of the resonance profile of the atomic transition (see fig. 3). For this, the Ti:Sapphire frequency is modulated at 138 Hz (with an amplitude of ≈ 200 kHz) and the recorded detection-region fluorescence is demodulated with a lock-in amplifier, whose output is fed back to the laser, through an electronic filter of low (≈ 1 Hz) bandwidth. This scheme ensures long-term frequency stability for the 408 nm laser system.

The 649 nm laser system, whose output is used to ex-

cite the 60 MHz wide $^3\text{P}_0 \rightarrow ^3\text{S}_1$ detection transition, is an external-cavity diode laser (Vitawave ECDL-6515R). To suppress frequency noise of this laser, its frequency is locked to the side-of-fringe of an airtight Fabry-Perot (FP) resonator. The resonator length is in turn stabilized with slow feedback to a set laser frequency, whose reading is made with a wavemeter (HighFinesse WSU2). This double-stage scheme ensures short- and long-term stability so that the impact of frequency excursions of the laser on the detection of the 408 nm transition is negligible.

Precise polarization control of the intracavity optical field, as well as continuous measurement of the PBC polarization, are needed in the experiment. The linear polarization of the light coupled to the PBC is set with a half-wave plate mounted on a motorized rotation stage. Measurements of the relative sizes of the three transition components in the 408 nm spectrum (see fig. 3) are used to read the intracavity light polarization angles θ_{\pm} (nominally $\pm\pi/4$) before the start of an experimental run (see Appendix B); these angles are correlated with the concurrent readings of a polarimeter measuring light transmitted through the PBC, whose subsequent readings during an experiment provide an accurate tracking of θ_{\pm} . The polarimeter makes use of a Glan-Taylor polarizer that analyzes a small fraction of the transmitted light intensity, picked off with a wedge window placed at near-normal incidence in the path of the beam exiting the PBC. The two orthogonal polarization states at the output of the polarizer are measured with a pair of amplified photodetectors. The polarizer axis is set so that the polarimeter is nominally balanced for the θ_{\pm} polarization angles. The small polarization ellipticity in the PBC, whose value is also required for an accurate PV-effect measurement, is determined using a scheme described in section IV A 2.

Lock-in amplifiers are used to measure the 1st and 2nd harmonics present in the 408 nm excitation rate (models Signal Recovery SR7265 and Zurich Instruments MLFI, respectively). For typical electric field amplitude $E_0 \approx 1$ kV/cm, the contribution to the ratio r_0 (12) from the PV effect is $4\zeta/\beta E_0 \approx 10^{-4}$. Due to the small size of the 1st harmonic $R_0^{[1]}$, its detection in the presence of a much larger 2nd harmonic amplitude $R_0^{[2]}$ is technically challenging. Two steps are taken to circumvent this issue. First, a field $E_{dc} \approx 6.3$ V/cm is applied in the interaction region. The resulting contribution $4E_{dc}/E_0$ to the ratio r_0 [see (12)], of typical value 0.02, is a purely PV-conserving signal, which does not affect the determination of the PV-related effect. The latter is determined through measurements of the change in r_0 with polarization angle θ . Second, the signal directed to the lock-in measuring $R_0^{[1]}$ is filtered with an amplified band-pass filter, which provides a gain of 101.67(22) for the 1st harmonic while attenuating the 2nd harmonic ≈ 50 times. These two steps result in $R_0^{[1]}$ and $R_0^{[2]}$ signals of comparable size presented to the respective lock-in amplifiers.

Finally, to avoid potential systematic effects due to the changing signal levels when measuring different isotopes, a variable-gain amplifier is used to adjust the signal level at the output of the detection-region photodetector. The gain values in this amplifier are related to the different isotopic abundances of the four Yb isotopes measured, such that the same signal level is always presented to the lock-ins, regardless of isotope measured.

IV. INVESTIGATION OF SYSTEMATIC EFFECTS AND RELATED ERRORS

In this section we present a detailed analysis of systematic contributions and uncertainties related to the isotopic comparison measurements. These uncertainties are either due to the limited accuracy of the various calibrations or imperfect estimates of the contribution of PV-mimicking effects. We begin by discussing the various PV-data calibrations and the errors in these, since the latter dominate the total systematic uncertainty in the present experiment. We then present an analysis of false-PV contributions and the related uncertainties. Finally, auxiliary experiments done to ensure consistency with our model of harmonics ratios, as well as to investigate potentially unaccounted-for systematics, are discussed at the end of the section.

A. Calibrations to PV-data and related uncertainties

1. 408 nm transition saturation

In the absence of saturation in the Stark-induced transition, the 408 nm signal grows as E^2 . In the present experiment the transition is weakly saturated. This slight saturation affects the measurement of the harmonics ratio r_0 , and a correction needs to be made. The transition rate can be generally expressed as:

$$R = \frac{kE^2}{1 + \frac{E^2}{E_s^2}}. \quad (15)$$

The parameter k is an overall constant (which depends on the light power in the PBC), E_s the saturation electric field, and $E = E_0 \cos \omega t + \zeta/\beta$ includes the applied electric field and the effective electric field ζ/β that results from the PV ($|\zeta/\beta| \ll E_0$). The field E_s depends on the intensity of the 408 nm light exciting atoms. The rate R is saturated when E_0 becomes comparable to E_s . In the present experiment, the 408 nm transition in the atomic beam is weakly saturated ($E_0/E_s \approx 0.1$). To quantify the impact on the harmonics ratio, we expand R in terms of the parameter $(E_0/E_s)^2$, and compute r_0 . To first order in this parameter, the modified ratio is:

$$r_0 = \frac{\zeta}{\beta E_0} \left(1 - \frac{1}{2} \frac{E_0^2}{E_s^2} \right). \quad (16)$$

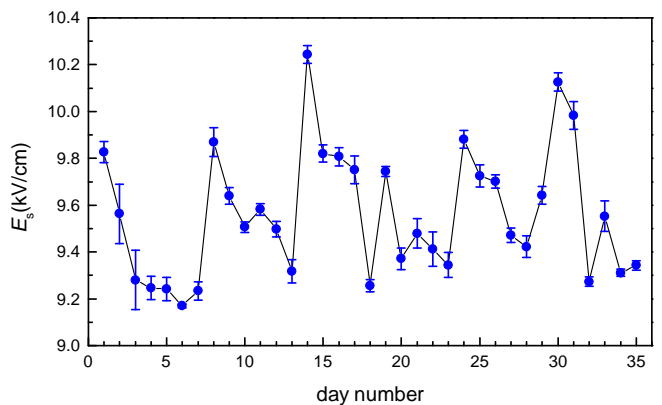


FIG. 4. (Color online) Measurements of the saturation electric field for the $0 \rightarrow 0$ component of the 408 nm transition, made on each of the 34 days in which PV-data were acquired. Each data point represents the average of four measurements, two of which were made for angle $\theta_+ = +\pi/4$ and another two for $\theta_- = -\pi/4$.

PV data need to be therefore divided by:

$$C_s = 1 - \frac{1}{2} \frac{E_0^2}{E_s^2}. \quad (17)$$

Similar analysis shows that the 2^{nd} harmonic in the transition rate is also diminished in the presence of saturation, by a factor $(1 - E_0^2/E_s^2)$.

In the presence of transition saturation, harmonics higher than the 2^{nd} emerge in the rate of eq. (15). We make use of a 4^{th} harmonic amplitude to measure the saturation parameter E_s . The ratio of 4^{th} to 2^{nd} harmonic amplitudes (to first order in $(E_0/E_s)^2$) is given by $E_0^2/4E_s^2$. Measurements of this ratio with varying E_0 (in the range 1-2.5 kV/cm) are made to determine E_s .

We show in fig. 4 measurements of the parameter E_s , made in each of the 34 days in which actual isotopic comparison PV-data were acquired. A periodic pattern can be observed in the data that involves a gradual decrease in E_s , followed by a recovery. This effect is currently not fully understood; however, as we observe, it is generally correlated with gradual deterioration of the in-vacuum PBC mirrors, in the presence of the intense near-UV light. Typically, operation of the PBC for a few days results in a decrease in the cavity finesse and power buildup of about 30%. The gradual decrease in E_s should be occurring due to an increase in the intra-cavity circulating power (which corresponds to an increase in the degree of saturation in the transition rate). Since the power transmitted through the PBC is actively stabilized, the observed effect implies that the transmission of the cavity output coupler gradually decreases. Recovery of the cavity mirrors is possible by exposing them to partial atmosphere (tens of mbar) for ≈ 1 min, in the presence of the intense 408 nm light. The recovery process generally results in an increase of E_s . We assume an error of 3% in the daily E_s value, to take into account possible drifts

of this parameter over the 8-16 hr long PV-run.

2. Polarization parameter p

The 408 nm polarization parameter p of eq. (14) needs to be precisely measured for an accurate ζ/β determination. For angles in the range $|\theta_{\pm}| = \pi/4 \pm 0.02$ and $|\phi_{\pm}| \leq 0.06$, this parameter can be approximated (with an error of a few parts per 10^5) as $p \approx p_{\theta} \cdot p_{\phi}$, with:

$$p_{\theta} = \cot \theta_{+} - \cot \theta_{-}, \quad (18)$$

$$p_{\phi} = \cos \phi_{+} - \cos \phi_{-}. \quad (19)$$

This separation of variables simplifies the determination of p . In the following, we discuss how p_{θ} and p_{ϕ} are measured.

The method of measuring θ is outlined in section III. First, we compare the amplitudes of the three peaks in the 408 nm spectrum (see fig. 3) to measure the polarization angle, and correlate this result with the reading of a polarimeter (thereby calibrating the polarimeter), whose subsequent measurements of the light transmitted through the PBC during a many-hour-long PV run provide a tracking of the angles θ_{\pm} . A detailed description of the method to determine the initial θ_{\pm} angles using the atoms as polarization probes, including the effects of apparatus imperfections, is given in Appendix B.

The uncertainty in p_{θ} has two contributions: the statistical uncertainty associated with the initial θ_{\pm} measurement using the atoms, and the systematic uncertainty arising from drifts in the readings of the polarimeter at the output of the PBC over a many-hour period. The statistical uncertainty (typically $<0.1\%$ of the PV effect) is added in quadrature with the statistical error in a block of data acquired in a daily run. To make an estimate for the systematic uncertainty, we took two long sets of polarization data. In these runs, following the initial correlation of the θ_{\pm} readings with the polarimeter readings, the p_{θ} measurements made with the two methods were compared over a period of 12 hours. These data are presented in fig. 5. During these runs, the PBC was unlocked several times, to investigate the effect of thermal cycles of the PBC optics on the actual polarization angle (read with the atoms), and well as on its measurement with the polarimeter. The data show that unlocking the PBC for minute-long periods of time, does have an impact on the intra-cavity polarization angle (fig. 5a). These polarization shifts are nevertheless tracked well by the polarimeter, as seen in fig. 5b. The relative drifts between the p_{θ} determinations made using the 408 nm resonance profile and those made using the polarimeter are always less than 10^{-3} of the nominal value $p_{\theta} = 2$. We assign a 10^{-3} fractional systematic uncertainty in determining p_{θ} .

The light ellipticity-related parameter p_{ϕ} is determined through measurements made using signals from

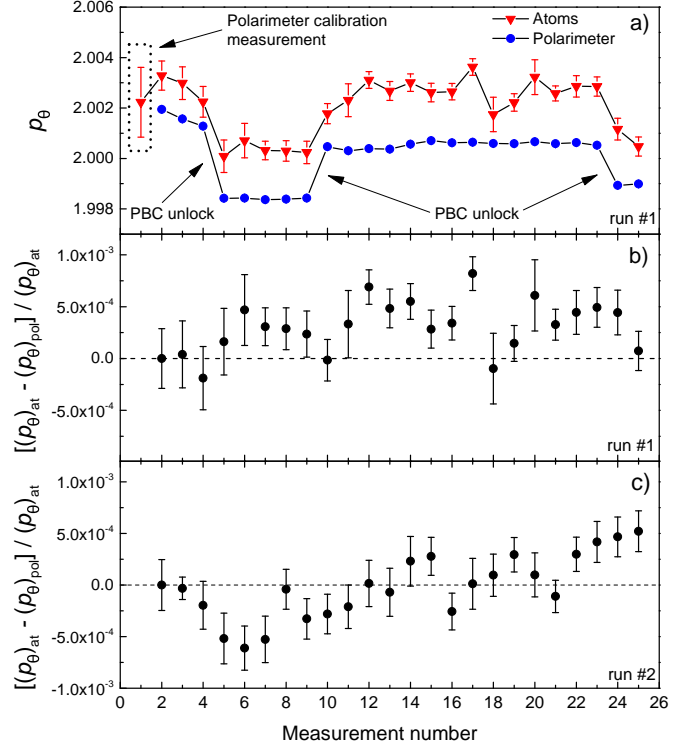


FIG. 5. (Color online) a) Comparison of p_{θ} measurements made with atoms and those made with the PBC polarimeter, over a 12 hr period. Error bars (smaller than data points for the polarimeter data) represent standard errors of the corresponding mean values. The first data point in the plot represents the initial reading of angles θ_{\pm} using the 408 nm spectrum. These readings are used to assign an initial value to the corresponding polarimeter readings. The statistical error in this first p_{θ} measurement explains the relative offset between the 'atoms' and 'polarimeter' points in the second measurement (points with measurement #2). The PBC was unlocked several times, with the duration of each pause in the range 5-10 min. Shorter (≈ 10 s) interruptions in the PBC lock were also made, and have no visible impact on polarization. b) Relative difference in p_{θ} readings between the two methods for the data shown in a). The offset between the 'atoms' and 'polarimeter' values at the start of the run (see points with measurement #2 in plot a)), is of statistical nature, and is removed in b), to allow for a study of relative drifts between the two determinations. c) Results of p_{θ} differences measured in another 12 hr-long run.

the atoms. The idea is to observe a term in the harmonics ratio of the $m' = \pm 1$ components of the 408 nm transition, that has a dependence on the angle ϕ . Expressions for the excitation rate for these components, as well as the corresponding harmonics ratios r_{+1} and r_{-1} in the presence of field imperfections, are given in Appendix A. The difference $r_{+1} - r_{-1}$ (retaining terms up to 2^{nd} order in the various field imperfections), is given by:

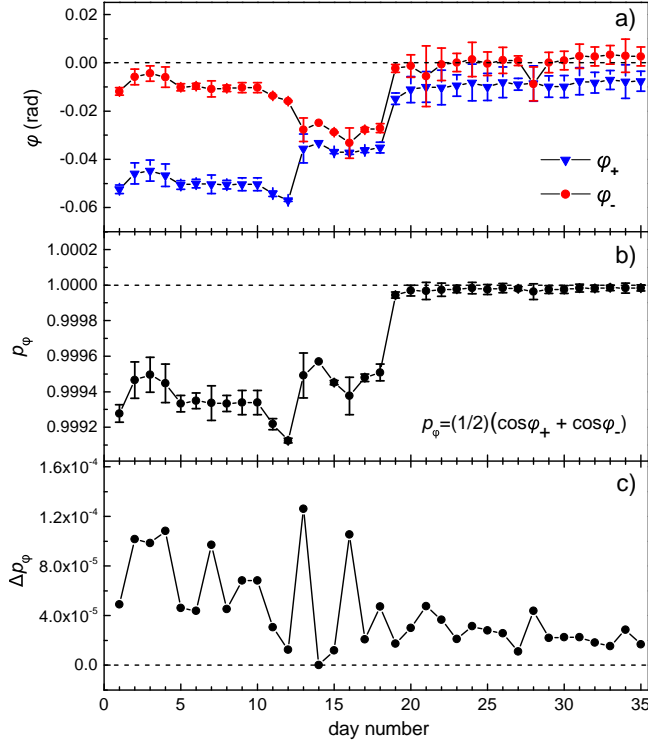


FIG. 6. a) (Color online) Angles ϕ_+ and ϕ_- determined on each of the 34 days of actual PV-data acquisition. Each data point represents the mean value of two measurements, of which the first was done before the start of the PV-run, and the second after the end of the run. The error bars correspond to the standard deviation of the mean. The changes in these values on days #13 and #18 are due to a readjustment of the tilt of the half-wave plate that controls the 408 nm light polarization coupled to the PBC. b) Corresponding p_ϕ parameter for the values shown in a). Error bars come from propagation of errors in the data points of a). c) Plot of the error-bar values for the data shown in b). The maximum error is $1.2 \cdot 10^{-4}$.

$$r_{+1} - r_1 = \frac{8e_z}{E_0} \tan \theta \sin \phi. \quad (20)$$

A measurement of r_{+1} and r_{-1} with an enhanced field component e_z , ($e_z/E_0 \approx \pm 0.06$) allows for extraction of ϕ_+ or ϕ_- , corresponding to polarization states with θ_+ or θ_- respectively. The overall accuracy is determined by statistics (the ratio e_z/E_0 is known to within 1%, and $\tan \theta$ is measured with sub-1% uncertainty).

Measurements of ϕ_\pm were made before the start and after the end of each of the many-hour-long PV-runs, employing both orientations of the magnetic field B_z . The ϕ_\pm value for the corresponding daily block of PV-data is taken as the mean of the initial and final measurements, and the error assigned to this mean is the standard deviation of the two values. We show the results of these measurements as well as resulting parameter p_ϕ and the error in its determination in fig. 6. We assign a fractional error of $1.2 \cdot 10^{-4}$ in the determination of p_ϕ . This

is a negligible contribution to the overall error in the polarization parameter p , an error dominated by the 10^{-3} fractional error in p_θ .

3. Effect of partial peak overlap

The applied magnetic field in the interaction region results in a resolved spectrum for the $^1S_0 \rightarrow ^3D_1$ transition (fig 3). A small residual overlap between the different peaks is still present, however, and its effect on the PV-measurements needs to be considered. In the presence of the overlap, the transition rate at the spectral peak position of the $0 \rightarrow 0$ transition component (where the PV-data are acquired) is given by:

$$R'_0 = R_0 + h \cdot R_{-1} + h \cdot R_{+1}. \quad (21)$$

The terms R_{-1} and R_{+1} are the rates of the $0 \rightarrow -1$ and $0 \rightarrow +1$ components, and h is a parameter that quantifies the contribution of the wing of a peak to the signal of the adjacent peak, measured to be $h = 4.2(4) \cdot 10^{-4}$. In formulating the total rate R'_0 in eq. (21), quantum interference between the transition amplitudes of the different Zeeman sub-levels is not considered. Such an effect does not take place in our system, since the emitted fluorescence light from de-excitation of atoms has different polarizations for the three excited-state sub-levels. Because of this, the corresponding excitation paths ($m = 0 \rightarrow m' = 0, \pm 1$) can be distinguished and amplitude interference does not occur. The resulting harmonics ratio r'_0 can be computed from (21), and from that, the corresponding combination K'_1 (Table I), can be determined:

$$K'_1 = \frac{16\zeta}{\beta} (1 - 2h). \quad (22)$$

To derive (22), field imperfections, which generally have a greater impact on the PV-measurements in the $0 \rightarrow \pm 1$ transitions, were neglected. This is a reasonable simplification. As discussed in section IV C 2, the PV-effect on the $0 \rightarrow \pm 1$ transitions, is, to within 2%, consistent in magnitude with the effect measured on the $0 \rightarrow 0$ transition. An additional 2% correction to the small calibration parameter of order h , would have a negligible impact on the PV-measurements taken on the $0 \rightarrow 0$ component. The negative sign in the signal contribution from the $0 \rightarrow \pm 1$ transitions is expected, since the PV-effect for these transitions is of opposite sign compared to that of the $0 \rightarrow 0$ component (see Appendix A). To correct for the effect of the partial overlap of the different Zeeman components in the $^1S_0 \rightarrow ^3D_1$ transition, the PV-measurements are divided by a factor $C_{\text{overlap}} = (1 - 2h)$.

4. Transit time from interaction to detection region

Due to the time required for excited atoms to reach the detection region and be measured, there is a phase delay in the detected excitation rate, relative to the electric field phase in the interaction region. This would not be an issue for a beam of atoms all moving with the same longitudinal velocity; however, because of the longitudinal velocity spread in the atomic beam, atoms in different velocity classes are detected at different times. This leads to a slight mixing of phases in the measured rate for these different classes, and to a frequency-dependent attenuation of the amplitude of each harmonic. The result of this attenuation is a detected harmonics ratio r_0 that is slightly larger than the actual one. This effect was modeled in [35]. We correct for it by dividing the measured r_0 by a factor $C_{transit}=1.00285(10)$. This factor is an order of magnitude lower than that in [35]. The reduction is due to the lower electric-field frequency (19.9 Hz) in the present experiment, compared to that of the previous one (76 Hz). The assigned error in $C_{transit}$ comes from the assumed uncertainty in the temperature of the Yb oven (± 50 °C) and from the assumed 0.5 cm uncertainty in the distance between the interaction and detection regions. The expected phase-delays in 1st and 2nd harmonic signals present in the transition rate (- 4.8° and - 9.6°) are detected correctly, to within 0.5°. A 0.5° error in the detected phase of a given harmonic in the excitation rate, would result in a fractional decrease of $5 \cdot 10^{-5}$ in the measured harmonic amplitude. The uncertainties in the measured PV effect arising from such small phase uncertainties in detecting the 1st and 2nd harmonics, are negligible.

5. Photodetector response calibration

The detection-region photodetector (PD) has a finite bandwidth, measured to be 1.1 kHz. The PD low-pass-filter behavior at the 1st- and 2nd- harmonic frequencies present in the transition rate (19.9 Hz and 39.8 Hz, respectively) is expected to have an impact on the measured ratio r_0 . To quantify this impact, we measured the frequency-dependent response of the PD, relative to that of a fast photodetector (Thorlabs PDA100, 220 kHz bandwidth). Using a light-emitting-diode as a source of sinusoidally modulated light, we measured with the PD a ratio of amplitudes at 39.8 Hz and 19.9 Hz, which was 1.00040(17) times greater than the ratio determined with the fast detector. The error in the measured amplitudes ratio is mainly statistical. The measured r_0 values are scaled down by $C_{PD}=1.00040(17)$ to compensate for the PD finite response time.

6. PD signal conditioning calibration

There is an overall calibration factor C_e relating the harmonics-ratio value recorded in the laboratory PC to the actual ratio at the output of the PD. This factor needs to be precisely measured. As part of the effort to improve detection conditions for the small 1st-harmonic signal in the transition rate, the PD signal is bandpass-amplified and then measured with a lock-in amplifier (see section III). The 1st-harmonic reading is recorded in the computer, as is the reading from another lock-in that measures the 2nd harmonic directly at the PD output. The calibration factor C_e was measured by replacing the PD with an electronic circuit that adds two known signals at the ω and 2ω frequencies. This circuit attenuates the ω signal to simulate the amplitude level in the actual experiment. The transfer function of this circuit for each of the two signal paths was measured at the 10^{-4} level. The inputs to the circuit come from a dual-channel function generator (Keysight 33510B) and are measured with a laboratory multimeter (Keysight 34410A), whose measurements agree with those made with an identical unit, at the 10^{-4} level. A comparison of the known harmonics ratio at the output of the adder-circuit, to the reading in the computer, determines C_e .

Many different measurements of C_e were made, with varying signal sizes as well as phase-delays between the lock-in reference phases and the corresponding detected phases. These measurements were carried out twice: before the start of the PV-data acquisition campaign, and after its end. The first measurement yielded a value $C_e=101.52(5)$ and a second a value $C_e=101.82(1)$. We assign the value of 101.67(22) to C_e , which is the mean of the two results. The 0.22% error in C_e is the standard deviation of the two measurements.

This inadvertent drift in the C_e calibration gives rise to the main systematic uncertainty in this experiment. Since the PV-data were acquired in a pattern that involved alternating measurements between isotopes, however, the impact of this drift on the actual isotopic comparison should be minimal.

7. Electric-field calibration

Accurate knowledge of the electric field applied to the atoms is needed to relate a determination of K_1 (see Table I) to the ratio ζ/β . There are two dominant uncertainties in the electric field. The first is an uncertainty in the calibration of the voltage monitor outputs in the two high-voltage amplifiers (model TREK 609B), used to apply voltage to the main field plates. The corresponding error in the applied voltage is a fractional $6 \cdot 10^{-4}$. The second uncertainty comes from imperfections in the construction of the field-plate system and the finite accuracy in measuring the field-plate spacing. This spacing was measured at several different places with a precision micrometer. The variation in the mean spacing (5.5045

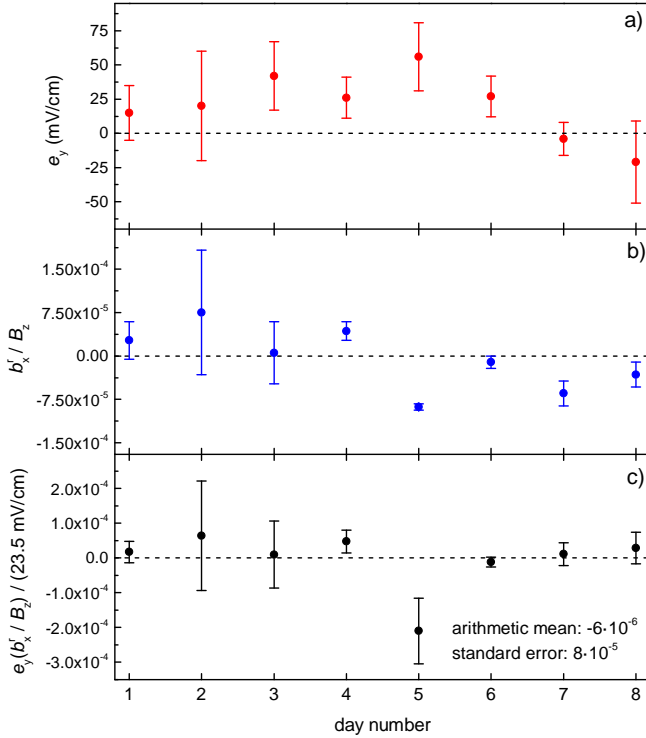


FIG. 7. (Color online) a) Measurements of the stray field e_y , made regularly during the isotopic comparison PV-run. This field is always 75 mV/cm or less in magnitude. b) Measured residual b_x^r/B_z values. The compensated ratio is stable at the 10^{-4} level. c) Fractional contribution of the $e_y b_x^r/B_z$ term to the measurement of the PV effect.

cm) was found to be 0.002 cm, which corresponds to a fractional uncertainty in the spacing of $\approx 4 \cdot 10^{-4}$, and to the same contribution to the overall electric field error.

B. False-PV signals and related uncertainties

In this subsection we discuss the methods to study and control known systematic contributions to the measurements which mimic the PV effect.

1. $e_y b_x^r$ contribution

Examination of the combination K_1 (Table I), shows that the coupling of a stray e_y field to the reversing magnetic field component b_x^r gives rise to the false-PV contribution proportional to $e_y b_x^r/B_z$, which directly competes with ζ/β . The strategy to handle this contribution is to minimize b_x^r , and then measure the residual effect periodically during the PV data acquisition, and, if needed, apply a correction to the PV-data.

To measure b_x^r we apply an enhanced e_y field, with $e_y/E_0 = \pm 0.062(1)$, and observe the change in K_1 as the polarity of this enhanced field is reversed. This allows one to isolate the $e_y b_x^r/B_z$ term and measure b_x^r/B_z .

The typical value for this misalignment is $1 - 2 \cdot 10^{-3}$. We then use shimming coils to apply a reversing field to null b_x^r . With this procedure the residual b_x^r/B_z ratio is measured to be 10^{-4} or less. We find that this cancellation is very stable with time (over month-long periods). Readjustment is only required when the alignment of the PBC optical axis (that defines the x-axis in the coordinate system) is changed. Such a change was only made once during the isotopic comparison data run.

With a suppressed b_x^r/B_z ratio, one has to monitor e_y during the PV-data campaign. To measure e_y we make use of the combination $K_3 = -16e_y b_x/E_0 B_z$. Another set of coils is used to apply an enhanced b_x , with $b_x/B_z \approx \pm 0.0390(6)$. Observation of the variation of K_3 with a sign flip in b_x/B_z is used to determine e_y .

We show measurements of e_y and the residual b_x^r/B_z ratio in fig. 7. These measurements were made concurrently, at regular intervals during the isotopic comparison PV run. The term $e_y b_x^r/B_z$ was never greater than $2 \cdot 10^{-4}$ of the measured PV-effect. The (arithmetic) mean value of the systematic is smaller than 10^{-5} . The error (standard error of the arithmetic mean) is less than 10^{-4} of the PV effect. We conclude that the contribution of this systematic to the PV measurements is negligible. We did not make use of weights in this statistical analysis, since the results of fig. 7 come from short acquisition runs, therefore the corresponding error bars may not represent errors accurately.

2. dK_1/db_x systematic

The $e_y b_x^r/B_z$ term is the only parasitic contribution in K_1 , within our model for the harmonics ratio, and up to 2^{nd} order in field imperfections. During auxiliary experiments that involved consecutive application of all possible field imperfections to the atoms, as a check for unaccounted-for systematic contributions, we discovered a dependence of K_1 on the non-reversing b_x component of the magnetic field. K_1 changes with b_x at a rate of $\approx 3\%/G$, for the $B_z=93$ G leading field. The origin of this effect is currently not understood. We did investigate its dependence on other parameters. No dependence was found on applied non-reversing or reversing electric-field components, or the amplitude of the leading electric field E_0 . We did observe a $\cot \theta$ dependence of the effect, like the PV effect itself has.

This spurious effect is periodically measured and corrections to the PV-data are made. To measure the residual b_x field, we make use of $K_3 \approx -16e_y b_x/B_z E_0$, in a manner similar to that described earlier for the measurements of the e_y field. Here we apply a known e_y , so that $e_y/E_0 \approx \pm 0.0644(10)$, and observe the change in K_3 , correlated with a polarity flip in e_y . In measurements made periodically during the PV-data run campaign, the observed b_x values were always smaller than 20 mG.

We show the measured dependence of K_1 on b_x in fig. 8a, along with calibration measurements of the spurious

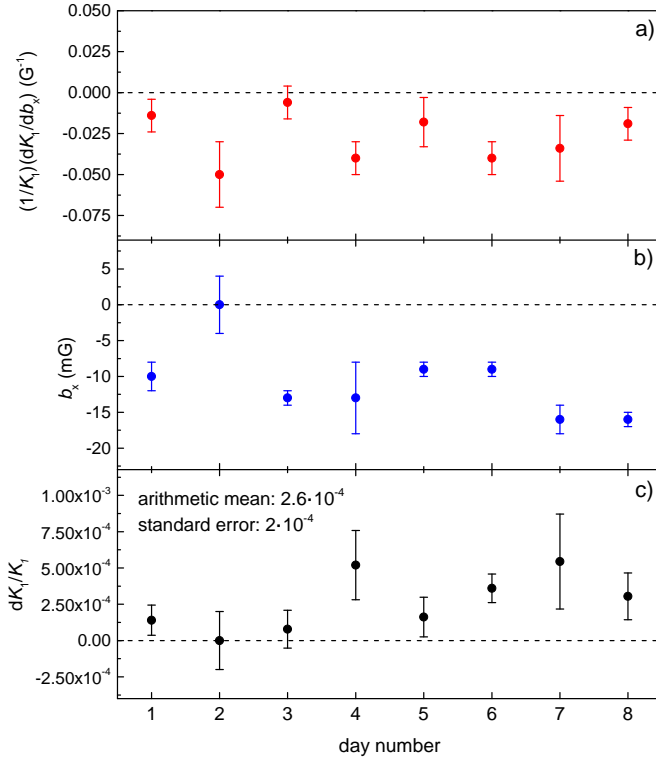


FIG. 8. (Color online) a) Fractional change in K_1 per G of the applied field b_x . b) Measured residual b_x field. c) Fractional change in K_1 , inferred from the data of a) and b).

effect in fig 8b. These data were taken regularly during the PV-data acquisition. The corresponding fractional K_1 change, inferred from the data of a) and b), is shown in fig. 8c. The arithmetic mean value of the change is $2.6 \cdot 10^{-4}$. We subtract this fraction from all PV data to account for this systematic effect, and assign a fractional uncertainty $2 \cdot 10^{-4}$, which represents the standard error of the arithmetic mean value. As in the studies related to the $e_y b_x^r/B_z$ systematic, use of weights in the statistical analysis is avoided.

3. E_{dc} and transition saturation

The E_{dc} field, applied to improve conditions in the Stark-PV interference detection, gives rise to a false-PV signal in the presence of saturation in the transition. To illustrate this, we consider the harmonics ratio of eq. (8):

$$r_0(\theta, f_B) = C_s \left(\frac{4E_{dc}}{E_0} + \frac{4\zeta}{\beta E_0} \cot \theta \right), \quad (23)$$

where C_s represents the slight saturation-related reduction in r_0 and is given by (17). This factor depends on the overall excitation rate. The corresponding combination K_1 is given by:

$$K_1 = \frac{16E_{dc}}{E_0}(C_{s+} - C_{s-}) + \frac{8\zeta}{\beta E_0}(\cot \theta_+ C_{s+} - \cot \theta_- C_{s-}). \quad (24)$$

The saturation factors C_{s+} and C_{s-} correspond to the two angles θ_+ and θ_- , respectively, and are generally slightly different. The quantity in parenthesis in the second term of (19) can be approximated as:

$$\frac{1}{2}(C_{s+} + C_{s-})(\cot \theta_+ - \cot \theta_-),$$

with an accuracy at the 10^{-5} level for angles $\theta_{\pm} \approx \pm\pi/4$ and the typical value ≈ 0.01 for C_{s+} and C_{s-} . The parameter K_1 can be then expressed as:

$$K_1 = \frac{16E_{dc}}{E_0}(C_{s+} - C_{s-}) + \frac{1}{2}(C_{s+} + C_{s-})\frac{8\zeta}{\beta E_0}(\cot \theta_+ - \cot \theta_-). \quad (25)$$

A small difference between C_{s+} and C_{s-} due to unequal excitation rates for the angles θ_+ and θ_- has no impact on the correction $(1/2)(C_{s+} + C_{s-})$ applied to the PV data, since the latter is determined using measurements made for both angles θ_{\pm} . Such a difference, however, introduces a false-PV signal proportional to E_{dc} . The fractional contribution of this systematic is:

$$\frac{E_{dc}}{\zeta/\beta} |C_{s+} - C_{s-}|. \quad (26)$$

During a PV-run we observe excitation rates for the two polarization angles θ_{\pm} which typically differ by $\approx 0.5\%$. This is because these angles are not precisely $\pm\pi/4$. Given that the saturation electric field E_s (17) grows as the square root of the signal, we can estimate that for the typical $E_0=1$ kV/cm and $E_s=10$ kV/cm, the quantity $|C_{s+} - C_{s-}| \approx 2.5 \cdot 10^{-5}$. Using the value of $|E_{dc}|=6.3$ V/cm of this experiment, and the measured $|\zeta/\beta| \approx 23.5$ mV/cm, we find that the false-PV term of (26) is a fractional 0.7%.

We handle this systematic by averaging PV-data taken with opposite E_{dc} polarities. The more precisely E_{dc} is reversed, the better the suppression of the related systematic. A good reversal is achieved with feedback on the E_{dc} value. To implement this, we make use of the combination K_4 (see table I), which, to an excellent approximation, is equal to $16E_{dc}/E_0$ (other terms in K_4 are suppressed by at least 10^4 times relative to this term). While data are being acquired, K_4 is monitored. Every time the E_{dc} polarity is flipped to negative, an adjustment is made to the new E_{dc} setting, to correct for small differences between the magnitudes of the previous two K_4 measurements, one of which corresponds to $E_{dc} > 0$ and the other to $E_{dc} < 0$. As a result, the total static field along x (i.e. the sum of the $|E_{dc}| \approx 6.3$ V/cm field and a stray field) is reversed to within 5-10 mV/cm, leading to a practically complete suppression of the related systematic effect.

C. ζ/β sign and consistency checks

In this sub-section we discuss the method to establish the sign of ζ/β . The present determination disagrees with that of the 2009 experiment [34, 35], which we have traced to a sign error in the analysis code employed in that work. We also provide the results of auxiliary experiments done to ensure consistency between measurements and our model for the expected PV effect.

1. ζ/β sign determination

The primary method to determine the sign of ζ/β is to study the sign of the term $(\zeta/\beta) \cot \theta$ in the harmonics ratio of (12), in relation to the signs of other terms in this ratio. The latter signs are unambiguously defined once the directions of the fields in the relevant terms are known. We focus this discussion on a sign-comparison between the PV-induced term in (12) and the terms that depend on the E_{dc} field as well as the PV-mimicking term $b_x e_y \cot \theta$. We consider the harmonics ratio r_0 of (12) :

$$r_0 = \frac{4E_{dc}}{E_0} + \frac{4\zeta}{\beta E_0} \cot \theta + \frac{4b_x e_y}{B_z E_0} \cot \theta, \quad (27)$$

where b_x and B_z are the total fields along x and z, and we have assumed no polarization ellipticity ($\phi = 0$). The contribution in r_0 from E_{dc} is sufficient to establish a sign definition for $(\zeta/\beta) \cot \theta$. We apply a large and positive E_{dc} , and adjust the phase of the lock-in amplifier that measures the 1st harmonic in the transition rate, such that the device output is maximum in magnitude and positive. (The phase of the lock-in measuring the 2nd is set so that its output always has the maximum magnitude and is positive.) The adjustment results in a positive result for r_0 . Reversing the E_{dc} polarity reverses the sign of r_0 . With this procedure, the sign of $(\zeta/\beta) \cot \theta$ is defined unambiguously. As long as the angle θ is set correctly, the sign of ζ/β can be determined by observing how r_0 changes with θ -reversals. Data that show dependence of r_0 on the polarity of E_{dc} as well as on θ , are presented in fig. 9.

We have further checked the sign of $(\zeta/\beta) \cot \theta$ relative to the term $(b_x/B_z)e_y \cot \theta$ of (27). By enhancing b_x and e_y , this term can be made rather large (up to 1000 ζ/β). It was confirmed that for $B_z > 0$ and enhanced $b_x > 0$ and $e_y > 0$, r_0 is positive when $\theta > 0$, and r_0 is negative when $\theta < 0$. A reversal of any of b_x , e_y or B_z causes r_0 to reverse sign (see fig 10a). This additional test is consistent with the sign definition based on the test with E_{dc} and furthermore, its result is consistent with our definition of the positive sense for the polarization angle θ . With a verified sign definition for θ , we further observed that the term $(\zeta/\beta) \cot \theta$ is of opposite sign compared to $(b_x/B_z)e_y \cot \theta$ for $B_z > 0$ and enhanced $b_x > 0$ and $e_y > 0$, therefore $\zeta/\beta < 0$ (see fig. 10b). Prior to these tests, and in fact prior to all the

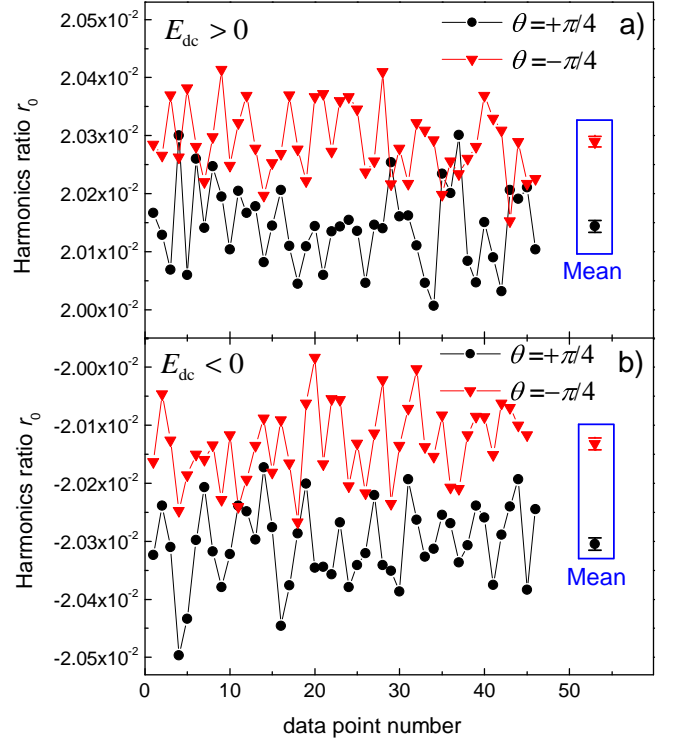


FIG. 9. (Color online) Harmonics ratio r_0 recorded in ^{172}Yb over a period of ≈ 25 min. Equal number of data points are shown for either orientation of the leading magnetic field B_z , and polarization angles $\theta_{\pm} \approx \pm\pi/4$. In a) the applied E_{dc} field, of approximate magnitude $|E_{dc}|=6.3$ V/cm, is positive, while in b) it is negative. The ac field applied to the atoms is of amplitude $E_0 \approx 1218$ V/cm. Observation of the change in r_0 with the E_{dc} -reversal establishes a sign definition for $(\zeta/\beta) \cot \theta$. Assuming θ is set in a way consistent with its sign definition (see coordinate system in fig. 2), then the observed dependence of r_0 on the θ -reversal, is sufficient to determine the ζ/β sign. The angle polarity is checked with measurements presented in fig.10. The difference in the mean r_0 ratios of a) and b) is $-2(8) \cdot 10^{-6}$, corresponding to a difference in the applied E_{dc} magnitudes of $-0.6(5)$ mV/cm, which is indicative of the quality of the E_{dc} reversal in the experiment.

PV experiments, it was confirmed that all the fields in the experiment (i.e. the voltage polarities of the 10 electrodes of our field plate system, the direction of the all the applied magnetic fields, and the polarization of the 408 nm light) are applied with correct polarity.

In addition to these tests, we made a makeshift measurement of the ratio of $M1$ transition moment to β , and compared our result with a prior determination of $M1/\beta$ [49]. This experiment required replacing the field plates shown in fig. 2 with others, which were oriented to create an electric field along z. Since the Stark- $M1$ interference is suppressed when atoms are excited by a standing-wave field, the PBC mirrors were removed for these measurements. The geometry of applied fields was the same as that employed in [49, 50]. Our result for

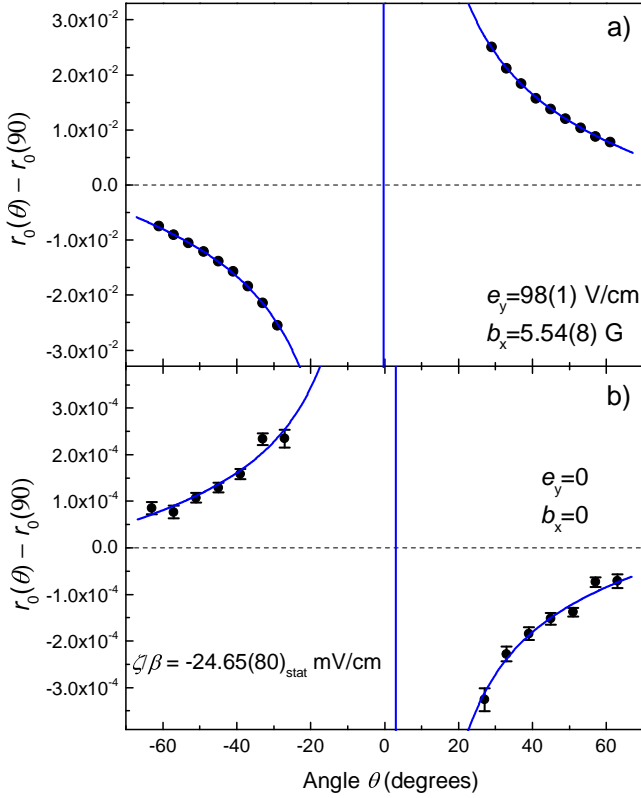


FIG. 10. (Color online) Harmonics ratio dependence on polarization angle, measured for ^{174}Yb , with a) application of enhanced field imperfections b_x and e_y (which are both positive as is the 93 G leading field B_z), resulting in a dominant contribution to r_0 from the term $(b_x/B_z)e_y \cot \theta$, b) without applied imperfections to the atoms, thus primarily observing the PV-related term $(\zeta/\beta) \cot \theta$. The measured ratio $r_0(\pi/2)$ is subtracted from data taken at other angles θ , to eliminate background signal which does not depend on θ . Error bars in a) are smaller than data points. The blue line in both plots is a fit to the data of the form $y = y_0 + A \cot(\theta - \theta_0)$. Observation of the change in the harmonics ratio with θ in a) offers a confirmation for the sign definition for θ . Furthermore, the θ -dependence of the ratio in b) provides an unambiguous determination of the sign of ζ/β . The data of b) also provide a measurement of ζ/β , which is consistent with the final result of $-23.90(11)$ mV/cm for the ^{174}Yb isotope.

$M1/\beta$ is $-23.46(100)$ V/cm, which agrees in sign with the previous result of $-22.3(10)$ V/cm, thereby offering additional assurance in our PV-effect sign determination. The quoted error in our measurement, of 1 V/cm is due to systematic uncertainty, primarily from the non-optimized construction of the field-plates used.

Finally, to ensure that our determination for the sign of ζ/β is free of possible errors in the computer code used to extract the PV parameter from raw data or other human error, two of us performed analyses of the same set of data with independently developed codes, and obtained the same results.

To further investigate the sign discrepancy we acquired

and analyzed data with ^{174}Yb using the methods employed in the previous experiment. For this we recorded with the new apparatus 408 nm transition lineshapes like that shown in fig. 3, under all combinations of parity-reversals employed in the 2009 work. One of us used the original data-analysis script written for the previous experiment, to perform lineshape fitting in the newly acquired spectra and extract the parameter ζ/β , exactly as it was done to obtain the results presented in [34, 35]. This analysis yielded a ζ/β value of $21.1(3.6)$ mV/cm, consistent in magnitude with the more accurate determination of $23.90(11)$ mV/cm that we report in this work for ^{174}Yb , but whose sign, however, was positive, just as the result reported in 2009. Examination of the data-processing script revealed that a minus sign was inadvertently omitted in the data analysis. Taking this omitted sign into account establishes consistency between the sign results of the 2009 experiment and our present measurements.

2. Other consistency checks

In addition to the auxiliary measurements related to the sign of the PV effect, a number of experiments were carried out to check for unaccounted-for systematic effects and ensure overall measurement consistency under various conditions.

Data were acquired with enhanced field imperfections, which were two to three orders of magnitude greater than those during actual PV-data acquisition, to check for the effects of potential field gradients. The results of these experiments (with uncertainty $\approx 2\%$ in the PV-effect) did not reveal the presence of unaccounted-for PV-mimicking effects, other than that described in section IV B 2. A set of PV runs was done with changing apparatus components, such as with different field plates and high-voltage amplifiers, and without the PBC cavity. These experiments were consistent with the final result for the PV effect. Several consistency checks were carried out, including measurements with the laser frequency tuned to the secondary peak of the $0 \rightarrow 0$, 408 nm transition profile (see fig. 3) and on the $0 \rightarrow \pm 1$ components of the transition. Fitting the transition lineshape to determine ζ/β (as in the 1st-generation experiment) was done to check for systematic effects associated with the transition profile. Data were also acquired on the $F = 1/2 \rightarrow F' = 1/2$ component of the ^{171}Yb 408 nm transition (F denotes the total angular momentum of a state), where there is no PV observable [48]. These consistency checks, to within their statistical uncertainty did not reveal unaccounted-for systematic effects. We list in Table II the results of some of the auxiliary experiments which were carried out.

Additional information about the consistency of the actual isotopic comparison data can be obtained from the analysis of the combinations of Table I. The quantity K_1 is used to determine the PV effect; K_4 is nominally invariant under the θ - and B -reversals, and is used to

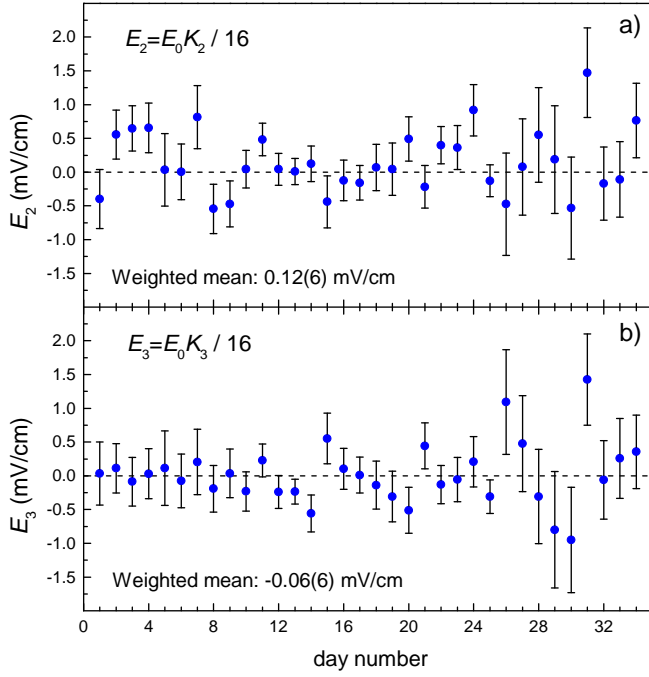


FIG. 11. (Color online) Effective electric field corresponding to the combination a) K_2 and b) K_3 (see table I). The data come from the isotopic comparison PV-run.

make a precise E_{dc} reversal during data acquisition. The combinations K_2 and K_3 are related to products of field imperfections (and ζ/β) and are expected to be small compared to the measured PV effect. We show in fig. 11 data related to K_2 and K_3 coming from the actual PV run on the four Yb isotopes. Since data were taken at different electric fields, instead of K_i , the effective electric field $E_i = E_0 K_i / 16$ ($i=2,3$) is shown in fig. 11, that can be directly compared to the determined effective PV field $|\zeta/\beta| \approx 23.5$ mV/cm. The weighted mean of E_3 is $\approx 0.26\%$ of $|\zeta/\beta|$ and consistent with zero within its 1σ uncertainty, and the weighted mean of E_2 is $\approx 0.51\%$ of $|\zeta/\beta|$ and consistent with zero within 2σ .

V. RESULTS AND ANALYSIS

In this section we present the results of the PV-isotopic comparison run that took place within a 2.5 month period, from 11/2017 to 01/2018. We compare the observed isotopic variation of the PV effect with the prediction of the SM for this variation. In addition, we present an analysis of these measurements, that is used to constrain electron-nucleon interactions due to the presence of an extra Z' boson.

A. Results of the PV-measurements

The results presented here are from data acquired on a chain of four Yb nuclear-spin-zero isotopes, with mass number $A=170, 172, 174, 176$, and abundance 3.1%, 21.9%, 31.8%, 12.9%, respectively. Measurements were made in 34 days, for a total of 260 hr of actual integration time (420 hr with $\approx 62\%$ measurement duty cycle). A typical routine in the experiment involved loading Yb metal into the oven, studying PV-mimicking systematics, followed by a five day measurement run, of an average 12 hr long daily data-taking time each day.

In each of a total of ≈ 900 PV-runs (each requiring $\approx 1/2$ hr), the harmonics ratio r_0 was measured on the $m = 0 \rightarrow m' = 0$ transition, a total of 200 times, under all polarity combinations of E, θ, B and E_{dc} , which were reversed at a rate of 19.9, 0.12, 0.06, and 0.03 Hz, respectively. The amplitude of the applied ac-field was $E_0 \approx 812$ or 1218 V/cm (1218 or 1624 V/cm with ^{170}Yb). We alternated data-taking between isotopes, to minimize the impact of potential drifts. The statistical error of the 30 min long PV run varied between 5% for the highest-abundance isotope (^{174}Yb) to 16% for the lowest-abundance (^{170}Yb).

The measured ζ/β value in each of the four isotopes, is shown in Table III. Our quoted result is the weighted mean of the set of measurements (PV runs) made on the particular isotope. The statistical uncertainty given in Table III is the standard error of the respective weighted mean. The systematic uncertainty of 0.06 mV/cm is the same for all isotopes. The main sources of this uncertainty were discussed in section IV, and their respective contributions are presented in Table IV.

Statistical consistency of the obtained sets of PV data is indicated by the resulting χ^2 value for each isotope, as well as by the probability value associated with the respective set. Consistency of the data is also supported by the frequency count plots of fig. 12, in which a random distribution of the measurements is observed.

The magnitude of ζ/β for ^{174}Yb was previously reported as $39(4)_{\text{stat}}(5)_{\text{syst}}$ mV/cm. That results differs from the present, much more accurate determination in the same isotope, by $\approx 2.4\sigma$. This discrepancy points to a possible underestimation of systematic uncertainties in the previous experiment. Note that the 1st-generation apparatus achieved an SNR in the measurements of the PV-effect, which was ≈ 18 times lower than that in the current experiment, thus making high-accuracy studies of systematic effects in the apparatus more difficult.

The observed signal-to-noise-ratio (SNR) in detection of the PV-effect was $0.55\sqrt{\tau}$ (τ is the integration time in s) for the highest-abundance isotope. This SNR is roughly consistent with shot-noise-limited detection of the 408 nm excitations in the atomic beam. To illustrate this, we compute the SNR for detection of the Stark-PV interference signal $S_{St-PV} = c_1 n \zeta \beta E_0$ in the presence of the Stark-induced signal $S_{St} = c_2 n \beta^2 E_0^2$. The parameter n is the atomic beam density, and c_1, c_2 are constants.

TABLE II. Results of auxiliary experiments

Isotope mass number	Transition	Conditions	ζ/β (mV/cm)
174	$m = 0 \rightarrow m' = 0$	Actual isotopic comparison data	-23.90(11)
174	$m = 0 \rightarrow m' = \pm 1$...	23.30(26) ^a
174	$m = 0 \rightarrow m' = 0$	Enhanced $e_y^r/E_0 = -0.03$	-24.30(48)
174	$m = 0 \rightarrow m' = 0$	Enhanced $e_y^r/E_0 = 0.03$	-23.93(40)
174	$m = 0 \rightarrow m' = 0$	Enhanced $e_z^r/E_0 = -0.029$	-23.98(57)
174	$m = 0 \rightarrow m' = 0$	Enhanced $e_z^r/E_0 = 0.029$	-23.76(57)
174	$m = 0 \rightarrow m' = 0$	Enhanced $e_z/E_0 = -0.076$	-24.67(57)
174	$m = 0 \rightarrow m' = 0$	Enhanced $e_z/E_0 = 0.076$	-23.83(57)
174	$m = 0 \rightarrow m' = 0$	Measurement on secondary transition peak	-24.14(44)
174	$m = 0 \rightarrow m' = 0, \pm 1$	Lineshape fitting	-21.100(360)
174	$m = 0 \rightarrow m' = 0$	r_0 vs. θ ^b	-24.65(80)
174	$m = 0 \rightarrow m' = 0$	Measurement without PBC	-26(7)
171	$F = 1/2 \rightarrow F' = 1/2$...	-0.59(57)
174	$m = 0 \rightarrow m' = 0$	408 nm excitation using circularly-polarized light	-0.2(1.2)

^a The PV-mimicking terms $e_y^r(e_z/E_0)$ and $e_z^r(e_y/E_0)$ were not compensated prior to the measurement (see Appendix A and eq. (A24)).

^b See fig. 10.

TABLE III. Results of PV measurements

Isotope mass number	Abundance (%)	Number of PV runs	ζ/β (mV/cm)	$\chi^2/\text{d.o.f.}$	p -value ^a
170	3.1	254	-22.81(22) _{stat} (0.06) _{syst}	1.09	0.16
172	21.9	199	-23.24(10) _{stat} (0.06) _{syst}	0.92	0.77
174	31.8	140	-23.89(11) _{stat} (0.06) _{syst}	0.99	0.53
176	12.9	291	-24.12(10) _{stat} (0.06) _{syst}	1.02	0.41

^a Probability that a repeated experiment would yield a χ^2 value greater than the observed one.

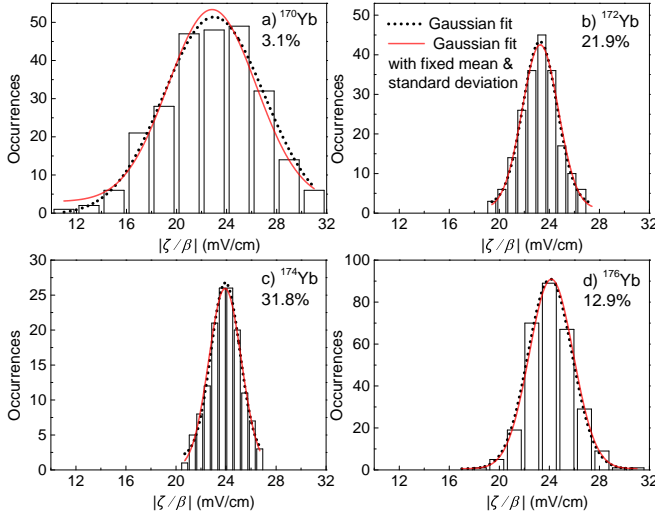


FIG. 12. (Color online) Occurrences of $|\zeta/\beta|$ values observed in 30-min long PV-runs, shown for each on the four Yb isotopes, whose respective abundances are given in the plots. The distribution of measurements is well-approximated by a Gaussian fit (dotted-black line), indicating that the PV-data are randomly distributed. Also shown in these plots is a solid-red line representing a Gaussian fit with fixed center and standard deviation. The center is the corresponding mean value from Table III and the standard deviation is the standard error of this mean multiplied by \sqrt{N} , where N is the number of data points (PV runs) given in Table III.

TABLE IV. Main systematic uncertainties in the PV measurements.

Contribution	Uncertainty(%)
Harmonics ratio calibration	0.22
Polarization angle	0.1
High-voltage measurements	0.06
Transition saturation correction	0.05 ^a
Field-plate spacing	0.04
Stray fields & field misalignments	0.02
Photo-detector response calibration	0.02

^a 0.09 for ^{170}Yb . The error is larger because part of the data for this low-abundance isotope were taken at a higher electric field.

The noise in detection of S_{St-PV} has three contributions: background (BG) noise (independent of S_{St}), technical noise $T \cdot S_{St}$ (i.e. proportional to the signal, with T a constant), and shot-noise $S\sqrt{S_{St}}$, where S is a constant. With quadrature addition of these contributions, we obtain for the SNR:

$$\begin{aligned}
 SNR &= \frac{S_{St-PV}}{\text{noise}} \\
 &= \frac{c_1 n \zeta \beta E_0}{\sqrt{BG^2 + S^2 c_2 n \beta^2 E_0^2 + T^2 c_2^2 n^2 \beta^4 E_0^4}}. \quad (28)
 \end{aligned}$$

When shot-noise is the dominant noise-source ($S^2 c_1 n \beta^2 E_0^2 \gg BG^2, T^2 c_2^2 n^2 \beta^4 E_0^4$), the SNR is given by:

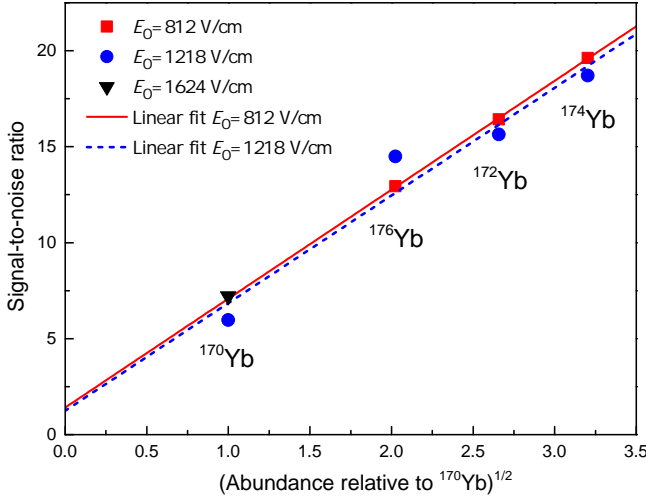


FIG. 13. (Color online) Obtained SNR in measurements of ζ/β in a 30 min long PV-run, plotted against the square root of the isotopic abundance (or equivalently, the effective atomic beam density). Values are shown for all three different electric fields for which data were taken. Each value in the plot is computed by multiplying the obtained standard error of the weighted mean value ζ/β in the corresponding set of data by \sqrt{N} , where N is the number of measurements in the set.

$$SNR \approx \frac{c_1 \zeta}{S \sqrt{c_2}} \sqrt{n}. \quad (29)$$

We see from (29) that the shot-noise-limited SNR does not depend on the electric field E_0 , and that it scales linearly with \sqrt{n} . Fig. 13 shows the observed SNR of a typical PV run per isotope and per value of E_0 . The SNR grows approximately as the square root of the isotope abundance, and it has little dependence on the electric field. These observations indicate that the detection of the PV effect approaches the shot-noise limit. Apparatus and measurement method-improvements that resulted in this sensitivity enhancement, relative to that in the 1st-generation experiment [34, 35], are discussed in [1].

B. Isotopic variation of the PV-effect and comparison with SM prediction

The uncertainty in the present measurements is low-enough to allow for observation of the isotopic variation of the PV effect, and a comparison of this variation with the related prediction of the SM. The effect predicted by the SM scales as the weak charge of the nucleus Q_W , which to lowest order in the SM is given by [2]:

$$Q_W = -N + Z(1 - 4 \sin^2 \theta_W), \quad (30)$$

where Z, N are the number of protons and neutrons in the nucleus and $\theta_W \approx 29.2^\circ$ is the weak-mixing angle

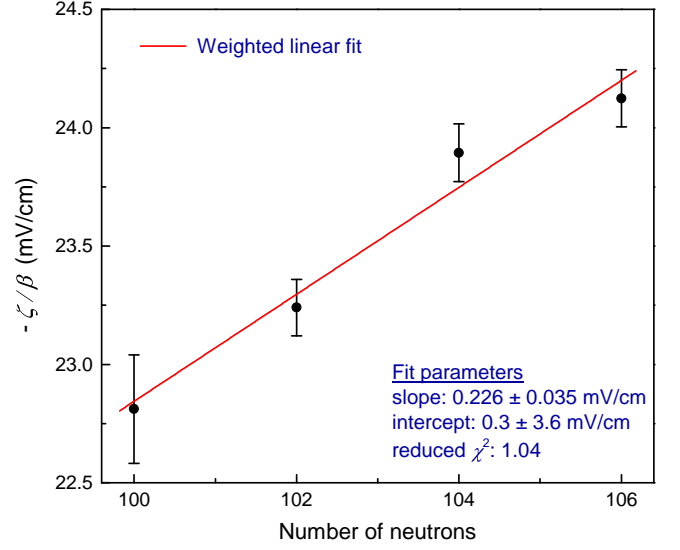


FIG. 14. (Color online) Isotopic variation of $-\zeta/\beta$. Error bars represent the statistical and systematic errors of Table III combined in quadrature. The weight assigned to each data point is the inverse square of the corresponding error bar shown in the plot. The intercept of the fitted line that depends on the contribution of the protons is small; it is consistent with the expected ≈ -1.2 mV/cm proton contribution to $-\zeta/\beta$, which provides additional confirmation that the effect measured in this experiment is indeed due to neutrons (i.e. due to the weak charge).

[51]. A more accurate expression for Q_W [51] is obtained with inclusion of radiative corrections:

$$Q_W \approx -0.989N + 0.071Z. \quad (31)$$

This expression should be accurate at the 0.1% level. For the mean neutron number $N = 103$ of the isotopes measured in this experiment, and $Z = 70$, the corresponding weak charge $Q_W = -96.88$, with a proton contribution $Q_p = 4.98$. About 95% of the Yb nucleus weak charge is carried by neutrons.

A clear variation of the measured PV-effect is seen in fig. 14, in which the determined $(-\zeta/\beta)$ values for the different isotopes vs. the neutron number are shown. This variation is determined from a weighted linear fit to the data, with a resulting fractional uncertainty of $\approx 15\%$. The y-intercept of the fitted line is consistent with the expected from the SM model contribution due to protons, estimated to be $(Q_p/Q_W) \cdot (-\zeta/\beta)_{N=103} \approx -1.2$ mV/cm with the value $(-\zeta/\beta)_{N=103} = 23.52$ mV/cm obtained from the fit parameters, and $Q_W = -96.88$ for $N=103$.

The measured fractional variation in the PV effect per neutron, around $N=103$, is $V_{exp} = \text{slope}/(-\zeta/\beta)_{N=103}$. From the parameters of the fit to the data of fig. 14, we obtain $V_{exp} = 0.96(15)\%$. Note that the estimated fractional change in the PV effect between the two extreme isotopes ^{170}Yb and ^{176}Yb , due to the variation in the neutron skin between these, is only about 0.1% [52], much

smaller than the observed change of $\approx 5.7\%$ between the two isotopes. The expected by the SM fractional variation in Q_W per neutron, around $N=103$ is:

$$V_{SM} = \frac{1}{Q_W} \frac{dQ_W}{dN} \approx 1\%. \quad (32)$$

The observed variation of the PV effect agrees well with the SM expectation, thus offering a direct confirmation of the Q_W dependence on neutrons.

The most precise determinations of a nuclear weak charge were made in ^{133}Cs ($Q_W = -72.58(43)$ [17]), ^{205}Tl ($Q_W = -113(3)$ [53]), and ^{208}Pb ($Q_W = -114(9)$) through a combination of measurements of the PV effect with atomic calculations. These determinations combined, have provided a test of the SM regarding the dependence of the weak charge on neutrons and protons. However, taking an agnostic approach, one may question if there is direct evidence of the weak charge being dominated by neutrons. Indeed, we can plot the value of the weak charge inferred from Cs, Tl and Pb experiments, and as a function of the number of neutrons (fig. 15a). The dependence is well fit with a linear function with the slope close to the expected value of ≈ -1 . However, a similar plot can also be drawn as a function of the proton number Z (fig. 15b), also displaying a good linear fit (which is not unexpected given the correlation between the number of protons and neutrons in atomic nuclei). Therefore, one can claim that the earlier experiments have not provided a model-independent way of showing that the weak charge is dominated by neutrons, the result we have been able to derive from the isotopic comparison in Yb.

C. Constraints on Z' bosons

As also discussed in [1] the results of the isotopic comparison can be used to place constraints on PV couplings between electrons and nucleons that are mediated by an extra vector boson Z' . A number of searches for light vector bosons of mass $m_{Z'} > 100$ keV, as well as searches for interactions of SM matter with dark-matter bosons and dark-energy fields have been reported (see, for example, review [4] and references therein). Constraints on Z' -mediated interactions were placed from torsion-pendulum [54, 55] and atomic-magnetometry [56] experiments, as well as from atomic calculations [25] that employed analyses of results of atomic PV experiments. These constraints are on combinations of electron-proton and electron-neutron PV interactions. The isotopic-comparison measurements allow for extraction of the proton contribution to the PV effect. This separation of the electron-proton PV coupling is used to provide individual constraints on an additional electron-proton PV interaction due to Z' exchange. These new constraints can be combined with existing upper bounds on the sum of electron-proton and electron-neutron couplings, to place a separate limit on electron-neutron interactions.

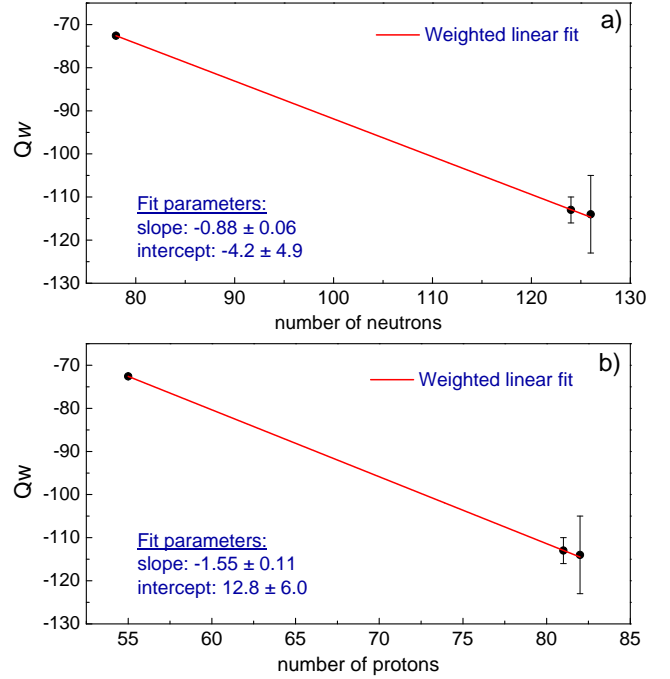


FIG. 15. (Color online) Nuclear weak charge plotted against a) number of neutrons and b) number of protons. The data points come from the most precise weak charge determinations, made in ^{133}Cs ($Z=55$, $N=78$), ^{205}Tl ($Z=81$, $N=124$), and ^{208}Pb ($Z=82$, $N=126$). The weight assigned to each point in order to perform a weighted linear fit to these data, is the inverse square of the corresponding error bar shown in the plot. Errors in the fit parameters are the 1σ errors.

The effects considered in the present analysis arise from the following interaction between the electron and nucleons:

$$\mathcal{L} = Z'_\mu \sum_{f=e,p,n} \bar{f} \gamma^\mu (g_f^V + \gamma_5 g_f^A) f. \quad (33)$$

The PV-induced transition moment in the presence of this additional interaction is given by [25]:

$$\zeta = E_\infty \left(\frac{-Q_W}{N} \right) + E(m_{Z'}) \frac{2\sqrt{2} A g_e^A g_N^V}{N G_F m_{Z'}^2}, \quad (34)$$

where $E(m_{Z'})$ is the calculated PV-induced amplitude arising from the interaction of (33) and E_∞ is the value of this amplitude for an interaction mediated by the SM Z boson which has a mass m_Z very large on the atomic scale. The parameter $G_F = 1.166 \cdot 10^{-5} \text{ GeV}^{-2}$ is the Fermi constant, and $g_e^A g_N^V$ is an effective axial electron-vector nucleon coupling, defined as:

$$g_e^A g_N^V \equiv \frac{Z}{A} g_e^A g_p^V + \frac{N}{A} g_e^A g_n^V, \quad (35)$$

where $A = Z + N$. The couplings $g_e^A g_p^V$ and $g_e^A g_n^V$ refer to the electron-proton and electron-neutron interactions, respectively. Their presence results in an additional contribution to the SM weak charge, such that

$Q_W = Q_W^{SM} + Q_W^{new}$, with:

$$Q_W^{new} = -\frac{E(m_{Z'})}{E_\infty} \frac{2\sqrt{2}Ag_e^A g_N^V}{G_F m_{Z'}^2}. \quad (36)$$

The amplitudes $E(m_{Z'})$ are calculated in [25], for several systems of interest for PV studies, for a range of masses 10 eV-1 GeV. These calculations are done using the same methods as those employed when calculating conventional atomic PV effects, with the exception that here the electron-nucleon PV potential, rather than being a contact potential, is allowed to have a finite range. The calculated amplitudes $E(m_{Z'})$ (given in Table I of ref. [25]), tend to a constant value in the low-mass limit $m_{Z'} < 100$ eV, while in the large-mass limit $m_{Z'} > 100$ MeV, they are proportional to $1/m_{Z'}^2$. Therefore these amplitudes are defined for any mass $m_{Z'}$.

We make use of the measured proton contribution to the PV effect to set limits on electron-proton interactions. This contribution is obtained from the fit to the data of fig. 14: $(-\zeta/\beta)_p = (0.3 \pm 3.6)$ mV/cm. With use of this value the proton part of the weak charge can be computed:

$$Q_p^{exp} = Q_W^{SM} \frac{(-\zeta/\beta)_p}{(-\zeta/\beta)}. \quad (37)$$

Using the value $Q_W^{SM} = -96.88$ and $(-\zeta/\beta) = 23.52$ mV/cm (obtained from the fit parameters of the plot of fig. (14) for N=103 neutrons), we obtain a measured proton weak charge $Q_p^{exp} = 1.24 \pm 14.83$. In deriving this value we did not consider the effects of the neutron skin and its variation across the chain of isotopes measured in this experiment. This is because the neutron-skin-related offset to $(-\zeta/\beta)_p$ is an estimated -0.4 mV/cm [52], much smaller than the 3.6 mV/cm error in the present $(-\zeta/\beta)_p$ determination. Using the computed Q_p^{exp} value, we place a limit on a potential beyond-SM proton contribution $Q_p^{new} = Q_p^{exp} - Q_p^{SM} = -3.75 \pm 14.83$. With the use of eq. (36), $g_e^A g_p^V$ is expressed as:

$$g_e^A g_p^V = -Q_p^{new} \frac{E_\infty}{E(m_{Z'})} \frac{G_F m_{Z'}^2}{2\sqrt{2}Z}. \quad (38)$$

Evaluation of eq. (38) with the calculated amplitudes $E(m_{Z'})$ for the Yb 408 nm transition, is employed to constrain the coupling $g_e^A g_p^V$ vs. $m_{Z'}$. These constraints are plotted in fig. 16a.

The obtained $g_e^A g_p^V$ constraints are combined [through eq. (35)] with existing constraints on the effective coupling $g_e^A g_N^V$, that come from the analysis of the results of the Cs PV experiment [15]. This analysis involves application of eq. (36) for the Cs $Q_W^{new}=0.65(43)$ [17] with use of the calculated Cs $6S \rightarrow 7S$ amplitudes $E(m_{Z'})$. This results in separate limits on the electron-neutron interaction $g_e^A g_n^V$, which are shown in fig. 16b.

The recent measurement of the weak charge of the proton in the Q-weak experiment [57], allows for tighter constraints on the $g_e^A g_p^V$ and $g_e^A g_n^V$ interactions, in the limit

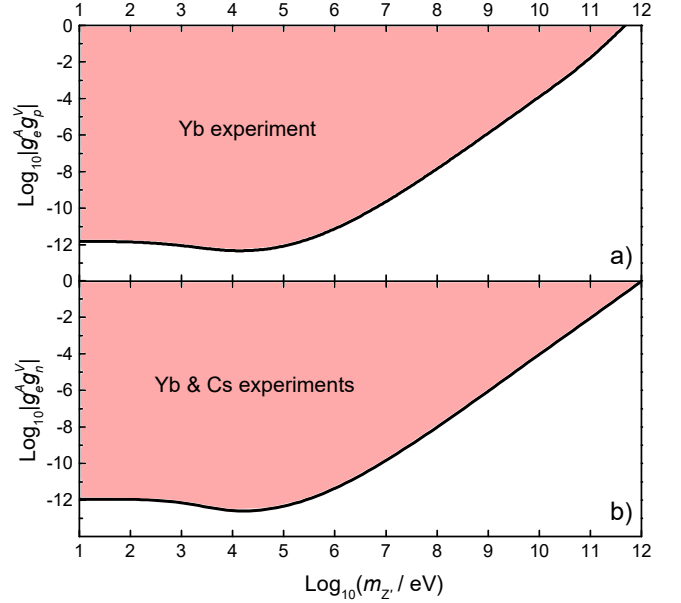


FIG. 16. (Color online) a) Bounds on light Z' -mediated PV electron-proton interactions. The black line represents the 1σ limit on the $g_e^A g_p^V$ coupling, shown for a large range of the boson mass $m_{Z'}$. The colored region indicates the parameter space excluded by the Yb experiment. The low-mass ($m_{Z'} < 100$ eV) limit for the coupling $|g_e^A g_p^V|$ is $1.6 \cdot 10^{-12}$ and the asymptotic large-mass ($m_{Z'} > 100$ MeV) limit is $|g_e^A g_p^V|/m_{Z'}^2 = 1.3 \cdot 10^{-6} (\text{GeV})^{-2}$. b) Bounds on light Z' -mediated PV electron-neutron interactions. The low-mass limit for the $|g_e^A g_n^V|$ interaction is $1.2 \cdot 10^{-12}$, and the corresponding large-mass asymptotic limit is $|g_e^A g_n^V|/m_{Z'}^2 = 9.3 \cdot 10^{-7} (\text{GeV})^{-2}$.

of a large mass for Z' ($m_{Z'} > 1$ GeV). That experiment provided bounds on a beyond-SM proton weak charge of $q_p^{new} = 0.0011(45)$. With $q_p^{new} = Q_p^{new}/Z$, we obtain from eq. (36) in the limit of large mass ($E(m_{Z'}) \rightarrow E_\infty$):

$$g_e^A g_p^V = -q_p^{new} \frac{G_F m_{Z'}^2}{2\sqrt{2}}. \quad (39)$$

With this constraint on $g_e^A g_p^V$ we once more make use of the existing bound on the effective coupling $g_e^A g_N^V$ from the Cs experiment and combine the two results to obtain a large-mass bound on $g_e^A g_n^V$. We list in Table V all small-mass and large-mass constraints derived by the analysis presented in this section.

VI. CONCLUSIONS AND OUTLOOK

We discussed in detail the experimental principle used to make improved measurements of the PV effect in a chain of four Yb isotopes. We described the 2nd-generation atomic beam apparatus, which offers enhanced sensitivity in the detection of the PV effect, thus

TABLE V. Upper bounds on electron-proton and electron-neutron interactions mediated by a vector boson Z' of mass $m_{Z'}$. These limits are derived through analysis of the results of different experiments or combinations of these. The large-mass limits $g_e^A g_p^V / m_{Z'}^2$ and $g_e^A g_n^V / m_{Z'}^2$ are valid for $m_{Z'} > 1$ GeV and the low-mass limits $g_e^A g_p^V$ and $g_e^A g_n^V$ for $m_{Z'} < 100$ eV (see table I in [25]).

Experiment	$g_e^A g_p^V / m_{Z'}^2 (\text{GeV})^{-2}$ (large-mass limit)	$g_e^A g_n^V / m_{Z'}^2 (\text{GeV})^{-2}$ (large-mass limit)	$g_e^A g_p^V$ (low-mass limit)	$g_e^A g_n^V$ (low-mass limit)
Yb PV	$(3.7 \pm 9) \cdot 10^{-7}$...	$(4.5 \pm 11) \cdot 10^{-13}$...
Yb & Cs PV	...	$(-2.9 \pm 6.4) \cdot 10^{-7}$...	$(-3.5 \pm 7.9) \cdot 10^{-13}$
Q-weak	$(-4.5 \pm 18.6) \cdot 10^{-9}$
Q-weak & Cs PV	...	$(-3.1 \pm 2.6) \cdot 10^{-8}$

enabling better characterization of systematic effects in these measurements. We gave a detailed account of the studies of these systematic effects, in relation to the isotopic-comparison experiment.

The results of the PV measurements presented here offer the first direct observation of isotopic dependence in atomic PV. The measured variation in the PV effect, of 0.96(15)% per neutron, is in agreement with the expectation based on the electroweak theory, of $\approx 1\%$ per neutron. Our result is consistent with the notion of the magnitude of the neutron weak charge being close to unity (Eq. (30)) and the weak charge of the nucleus to be additive over the neutrons.

The isotopic-comparison method allowed the extraction of the proton contribution to the PV effect. This contribution has enabled analysis that provided constraints on axial electron-vector proton interactions, mediated by a light boson Z' . These new constraints were combined with existing constraints on the sum of electron-proton and electron-neutron couplings, to provide separate constraints on the latter.

The attained single-isotope uncertainty is $\approx 0.5\%$ for three of the Yb isotopes measured. This level of accuracy is comparable to that of the most precise experiment to date, conducted in Cs (0.35% [15]). The present sensitivity level is a benchmark for the newly-built apparatus. Many avenues to enhance sensitivity have been identified and are currently being explored. These include an increase in the atomic beam flux, laser cooling of the atomic beam, optical pumping of the nonzero nuclear spin isotopes, and upgrade of the PBC cavity for a greater circulating power level. These upgrades are expected to enhance the sensitivity to a level that will enable high-precision isotopic comparison to probe the neutron distributions in the Yb nucleus and, potentially, physics beyond the Standard Model with use of the isotopic comparison method [22, 24]. The latter searches should not be hindered by uncertainties in the knowledge of the Yb nucleus neutron skin [52]. In addition, our planned investigation of spin-dependent PV through a comparison of the effect among the different hyperfine levels of the forbidden transition in the non-zero-spin iso-

topes is expected to improve the understanding of the intranuclear weak forces.

An increase in the experimental sensitivity must be accompanied by improved understanding and control of systematic effects. With consideration to improved isotopic comparison measurements on a chain of nuclear-spin-zero isotopes, systematic effects should not pose substantial difficulties. This is because the energy level structure is identical for the different isotopes, and since the influence of such spurious effects on measurements made on the $\Delta m = 0$ transition is only moderate. The various calibrations applied to the data, as well as the associated uncertainties, are also largely independent of isotope measured.

Greater attention to systematics is required in the studies of spin-dependent PV. It is possible that some effects could contribute differently among the different hyperfine transitions, and affect the results of hyperfine comparison. A substantial amount of related studies was done in the Cs experiment [15], which (similarly to the present work) employed the Stark-PV interference method and was done with an atomic beam, with the use of a standing-wave field to excite atoms. Systematic contributions influencing the hyperfine comparison in that work came from the presence of a $M1$ transition amplitude, which, although suppressed due to the use of a standing-wave, was allowed by the geometry of applied fields. In the Yb experiment, in addition to the suppression provided by the PBC, the experimental geometry is such that the Stark and $M1$ amplitudes are out of phase for the $\Delta m = 0$ transition that we employ, and therefore they do not interfere. In addition to $M1$ -related systematics, the effects of an electric-quadrupole ($E2$) transition between the 1S_0 and 3D_1 states need to be considered. The $E2$ transition is weakly allowed in the nonzero-spin isotopes due to hyperfine interaction-induced mixing between the 3D_1 and 3D_2 states. A detailed evaluation of the $E2$ amplitudes in the $^1S_0 \rightarrow ^3D_1$ transition was reported in [58]. Fortunately, the same mechanisms employed to suppress the Stark and $M1$ effects in PV measurements (experimental field geometry, excitation with counter-propagating light beams, selec-

tion of $\Delta m = 0$ transitions), are expected to provide adequate suppression of Stark- $E2$ signal contributions in the nonzero-spin isotopes. Modeling of systematics in these isotopes, just as it was done for the studies presented here, shows that parasitic contributions to the true PV signal should be similar to those in the spin-zero isotopes. While the analysis indicates that it should be possible to control systematics in the measurements of the nuclear-spin-dependent PV, we expect that during the course of the Yb PV program, studies of systematics

will require most of our attention.

ACKNOWLEDGEMENTS

We are grateful to M. Safronova, M. Kozlov, S. Porsev, M. Zolotarev, A. Viatkina, L. Bougas and N. Leefer for fruitful discussions. VF thanks Gutenberg Fellowship and Australian Research Council. AF is supported by the Carl Zeiss Graduate Fellowship.

-
- [1] D. Antypas, A. Fabricant, J. E. Stalnaker, K. Tsigutkin, V. V. Flambaum, and D. Budker, *Nat. Phys.* **15**, 120 (2019).
 - [2] J. S. Ginges and V. V. Flambaum, *Phys. Rep.* **397**, 63 (2004).
 - [3] B. Roberts, V. Dzuba, and V. Flambaum, *Ann. Rev. Nucl. Part. Sci.* **65**, 63 (2015).
 - [4] M. S. Safronova, D. Budker, D. DeMille, D. F. J. Kimball, A. Derevianko, and C. W. Clark, *Rev. Mod. Phys.* **90**, 025008 (2018).
 - [5] M. A. Bouchiat and C. C. Bouchiat, *Phys. Lett. B* **48**, 111 (1974).
 - [6] Y. B. Zel' Dovich, *J. Exptl. Theoret. Phys. (U.S.S.R.)* **36**, 964 (1959).
 - [7] L. M. Barkov and M. S. Zolotarev, *JETP Lett.* **27**, 357 (1978).
 - [8] R. Conti, P. Bucksbaum, S. Chu, E. Commins, and L. Hunter, *Phys. Rev. Lett.* **42**, 343 (1979).
 - [9] M. A. Bouchiat, J. Guena, L. Pottier, and L. Hunter, *Phys. Lett. B* **117**, 358 (1982).
 - [10] M. J. D. MacPherson, K. P. Zetie, R. B. Warrington, D. N. Stacey, and J. P. Hoare, *Phys. Rev. Lett.* **67**, 2784 (1991).
 - [11] D. M. Meekhof, P. Vetter, P. K. Majumder, S. K. Lamoreaux, and E. N. Fortson, *Phys. Rev. Lett.* **71**, 3442 (1993).
 - [12] S. J. Phipp, N. H. Edwards, E. G. Baird, and S. Nakayama, *J. Phys. B: At. Mol. Opt. Phys.* **29**, 1861 (1996).
 - [13] P. A. Vetter, D. M. Meekhof, P. K. Majumder, S. K. Lamoreaux, and E. N. Fortson, *Phys. Rev. Lett.* **74**, 2658 (1995).
 - [14] N. H. Edwards, S. J. Phipp, P. E. Baird, and S. Nakayama, *Phys. Rev. Lett.* **74**, 2654 (1995).
 - [15] C. S. Wood, S. C. Bennett, D. Cho, B. P. Masterson, J. L. Roberts, C. E. Tanner, and C. E. Wieman, *Science* **275**, 1759 (1997).
 - [16] J. Guéna, M. Lintz, and M. A. Bouchiat, *Phys. Rev. A* **71**, 042108 (2005).
 - [17] V. A. Dzuba, J. C. Berengut, V. V. Flambaum, and B. Roberts, *Phys. Rev. Lett.* **109**, 203003 (2012).
 - [18] V. V. Flambaum and I. B. Khriplovich, *ZhETF* **79**, 1656 (1980).
 - [19] V. V. Flambaum and I. B. Khriplovich, *JETP* **52**, 835 (1980).
 - [20] V.V. Flambaum, I.B. Khriplovich, and O.P. Sushkov, *Phys. Lett. B* **146(6)**, 367 (1984).
 - [21] B. Desplanques, J. F. Donoghue, and B. R. Holstein, *Ann. Phys.* **124**, 449 (1980).
 - [22] V. A. Dzuba, V. V. Flambaum, and I. B. Khriplovich, *Z. Phys. D* **1**, 243 (1986).
 - [23] E. N. Fortson, Y. Pang, and L. Wilets, *Phys. Rev. Lett.* **65**, 2857 (1990).
 - [24] A. V. Viatkina, D. Antypas, M. G. Kozlov, D. Budker, and V. V. Flambaum, *arXiv:1903.00123 [physics.atom-ph]* (2019).
 - [25] V. A. Dzuba, V. V. Flambaum, and Y. V. Stadnik, *Phys. Rev. Lett.* **119**, 223201 (2017).
 - [26] J. Zhang, R. Collister, K. Shiells, M. Tandecki, S. Aubin, J. A. Behr, E. Gomez, A. Gorelov, G. Gwinner, L. A. Orozco, M. R. Pearson, and Y. Zhao, *Hyperfine Interact.* **237**, 150 (2016).
 - [27] T. Aoki, Y. Torii, B. K. Sahoo, B. P. Das, K. Harada, T. Hayamizu, K. Sakamoto, H. Kawamura, T. Inoue, A. Uchiyama, S. Ito, R. Yoshioka, K. S. Tanaka, M. Itoh, A. Hatakeyama, and Y. Sakemi, *Appl. Phys. B* **123**, 120 (2017).
 - [28] M. Nuñez Portela, E. A. Dijck, A. Mohanty, H. Bekker, J. E. Van Den Berg, G. S. Giri, S. Hoekstra, C. J. Onderwater, S. Schlessler, R. G. Timmermans, O. O. Versolato, L. Willmann, H. W. Wilschut, and K. Jungmann, *Appl. Phys. B* **114**, 173 (2014).
 - [29] J. Choi and D. S. Elliott, *Phys. Rev. A* **93**, 023432 (2016).
 - [30] N. Leefer, L. Bougas, D. Antypas, and D. Budker, *arXiv:0912.2133 [physics.atom-ph]* (2014).
 - [31] A. Nuyen, D. Budker, D. DeMille, and M. Zolotarev, *Phys. Rev. A* **56**, 3453 (1997).
 - [32] E. Altuntas, J. Ammon, S. B. Cahn, and D. DeMille, *Phys. Rev. Lett.* **120**, 142501 (2018).
 - [33] E. Altuntas, J. Ammon, S. B. Cahn, and D. Demille, *Phys. Rev. A* **97**, 042101 (2018).
 - [34] K. Tsigutkin, D. Dounas-Frazer, A. Family, J. E. Stalnaker, V. V. Yashchuk, and D. Budker, *Phys. Rev. Lett.* **103**, 071601 (2009).
 - [35] K. Tsigutkin, D. Dounas-Frazer, A. Family, J. E. Stalnaker, V. V. Yashchuk, and D. Budker, *Phys. Rev. A* **81**, 032114 (2010).
 - [36] D. DeMille, *Phys. Rev. Lett.* **74**, 4165 (1995).
 - [37] S. Porsev, Y. G. Rakhlin, and M. Kozlov, *JETP Letters* **61**, 459 (1995).
 - [38] B. P. Das, *Phys. Rev. A* **56**, 1635 (1997).
 - [39] V. A. Dzuba and V. V. Flambaum, *Phys. Rev. A* **83**, 042514 (2011).
 - [40] M. A. Bouchiat and C. Bouchiat, *J. Phys.* **36**, 493 (1975).
 - [41] M. Bouchiat and L. Pottier, *Science* **234**, 1203 (1986).

- [42] P. S. Drell and E. D. Commins, Phys. Rev. Lett. **53**, 968 (1984).
- [43] C. J. Bowers, D. Budker, S. J. Freedman, G. Gwinner, J. E. Stalnaker, and D. DeMille, Phys. Rev. A **59**, 3513 (1999).
- [44] J. E. Stalnaker, D. Budker, S. J. Freedman, J. S. Guzman, S. M. Rochester, and V. V. Yashchuk, Phys. Rev. A **73**, 043416 (2006).
- [45] D. R. Dounas-Frazer, K. Tsigtukin, A. Family, and D. Budker, Phys. Rev. A **82**, 062507 (2010).
- [46] D. Antypas, A. Fabricant, and D. Budker, Opt. Lett. **43**, 002241 (2018).
- [47] D. Antypas, A. Fabricant, L. Bougas, K. Tsigtukin, and D. Budker, Hyperfine Interact. **238**, 21 (2017).
- [48] K. Tsigtukin, J. E. Stalnaker, D. Budker, S. J. Freedman, and V. V. Yashchuk, in *Proceedings of The 3rd Workshop From Parity Violation to Hadronic Structure and more...* (2006).
- [49] J. E. Stalnaker, D. Budker, D. P. DeMille, S. J. Freedman, and V. V. Yashchuk, Phys. Rev. A **66**, 031403 (2002).
- [50] D. Budker and J. E. Stalnaker, Phys. Rev. Lett. **91**, 263901 (2003).
- [51] M. Tanabashi *et al.*, Phys. Rev. D **98**, 030001 (2018).
- [52] B. A. Brown, A. Derevianko, and V. V. Flambaum, Phys. Rev. C **79**, 035501 (2009).
- [53] M. G. Kozlov, S. G. Porsev, and W. R. Johnson, Phys. Rev. A **64**, 052107 (2001).
- [54] B. R. Heckel, C. E. Cramer, T. S. Cook, E. G. Adelberger, S. Schlamminger, and U. Schmidt, Phys. Rev. Lett. **97**, 021603 (2006).
- [55] B. R. Heckel, E. G. Adelberger, C. E. Cramer, T. S. Cook, S. Schlamminger, and U. Schmidt, Phys. Rev. D **78**, 092006 (2008).
- [56] G. Vasilakis, J. M. Brown, T. W. Kornack, and M. V. Romalis, Phys. Rev. Lett. **103**, 261801 (2009).
- [57] D. Androic *et al.*, Nature **557**, 207 (2018).
- [58] M. G. Kozlov, V. A. Dzuba, and V. V. Flambaum, Phys. Rev. A **99**, 012516 (2019).
- [59] M. A. Bouchiat, A. Coblentz, J. Guéna, and L. Pottier, J. Phys. **42**, 985 (1981).

Appendix A: Transition rates and ratios $r_{m'}$ for the $m = 0 \rightarrow m' = 0, \pm 1$ transitions

The amplitudes for the Stark-, PV-induced and magnetic-dipole ($M1$) transitions between the $^1S_0, m = 0 \rightarrow ^3D_1, m' = 0, \pm 1$ states are given by [35]:

$$A_{m'}^{Stark} = i\beta(-1)^{m'}(\vec{E} \times \vec{\mathcal{E}})_{-m'}, \quad (A1)$$

$$A_{m'}^{PV} = i\zeta(-1)^{m'}\vec{\mathcal{E}}_{-m'}, \quad (A2)$$

$$A_{m'}^{M1} = M1(-1)^{m'}(\hat{k} \times \vec{\mathcal{E}})_{-m'}, \quad (A3)$$

where \hat{k} is the unit vector related to the optical field with electric field amplitude $\vec{\mathcal{E}}$, and $M1$ is the magnetic-dipole transition moment, measured in [49]: $|M1| = 1.33(21) \times 10^{-4} \mu_B$, where μ_B is the Bohr magneton. The geometry

of applied fields in the present experiment, however, is such that A^{M1} is out of phase with respect to A^{Stark} , such that the two amplitudes do not interfere. A second level of suppression is due to the standing-wave nature of the optical field in the PBC [59]. As discussed in [35], the $M1$ amplitude in the presence of a standing-wave with counter-propagating field amplitudes $\vec{\mathcal{E}}_+$ and $\vec{\mathcal{E}}_-$, is given by:

$$A_{m'}^{M1,PBC} = M1(-1)^{m'}(\kappa \hat{k} \times \vec{\mathcal{E}})_{-m'}, \quad (A4)$$

where $\vec{\mathcal{E}} = \vec{\mathcal{E}}_+ + \vec{\mathcal{E}}_-$ and $\kappa = (\mathcal{E}_+ - \mathcal{E}_-)/\mathcal{E}$. The amplitude of (A4) is suppressed by a factor $1/\kappa$, relative to that induced by a traveling-wave field. The suppression is ≈ 300 in the present experiment. We do include $A_{m'}^{M1,PBC}$ in our model for the harmonics ratio, and find that its contribution as a PV-mimicking effect is negligible.

We first consider the ideal case, in which there are no stray-fields, field misalignments, or ellipticity in the optical field polarization and $\kappa = 0$, and derive expressions for the three frequency components $R_{m'}^{[0]}$, $R_{m'}^{[1]}$, and $R_{m'}^{[2]}$ present in the excitation rate $R_{m'}$. In this case, the electric, magnetic, and optical fields are as follows:

$$\vec{E} = (E_{dc} + E_0 \cos \omega t)\hat{x}, \quad (A5)$$

$$\vec{B} = B_z \hat{z}, \quad (A6)$$

$$\vec{\mathcal{E}} = \mathcal{E}(\sin \theta \hat{y} + \cos \theta \hat{z}). \quad (A7)$$

The transition rate $R_{m'}$ is given by:

$$R_{m'} \propto |A_{m'}^{Stark} + A_{m'}^{PV}|^2 \quad (A8)$$

$$= R_{m'}^{[0]} + R_{m'}^{[1]} \cos \omega t + R_{m'}^{[2]} \cos 2\omega t. \quad (A9)$$

Evaluating the amplitudes of (A1, A2 and A4) in (A8) yields the following harmonic amplitudes for the $0 \rightarrow 0$ transition rate:

$$R_0^{[0]} \approx 2\mathcal{E}^2 \beta^2 E_0^2 \sin^2 \theta + 4\mathcal{E}^2 \beta^2 E_{dc}^2 \sin^2 \theta + 8\mathcal{E}^2 \beta E_{dc} \zeta \cos \theta \sin \theta, \quad (A10)$$

$$R_0^{[1]} = 8\mathcal{E}^2 \beta E_0 \zeta \cos \theta \sin \theta + 8\mathcal{E}^2 \beta^2 E_0 E_{dc} \sin^2 \theta, \quad (A11)$$

$$R_0^{[2]} \approx 2\mathcal{E}^2 \beta^2 E_0^2 \sin^2 \theta. \quad (A12)$$

The amplitudes for the $0 \rightarrow \pm 1$ transitions are:

$$R_{\pm 1}^{[0]} \approx \mathcal{E}^2 \beta^2 E_0^2 \cos^2 \theta + 2\mathcal{E}^2 \beta^2 E_{dc}^2 \cos^2 \theta - 4\mathcal{E}^2 \beta E_{dc} \zeta \cos \theta \sin \theta, \quad (A13)$$

$$R_{\pm 1}^{[1]} = -4\mathcal{E}^2 \beta E_0 \zeta \cos \theta \sin \theta + 4\mathcal{E}^2 \beta^2 E_0 E_{dc} \cos^2 \theta, \quad (A14)$$

$$R_{\pm 1}^{[2]} = \mathcal{E}^2 \beta^2 E_0^2 \cos^2 \theta. \quad (\text{A15})$$

The terms proportional to ζ^2 were dropped in (A10, A12, A13). The apparatus measures the ratio of the 1st- to the 2nd harmonic in the transition rate. When exciting the $0 \rightarrow 0$ transition, this ratio is given by:

$$r_0 \equiv \frac{R_0^{[1]}}{R_0^{[2]}} = \frac{4E_{dc}}{E_0} + \frac{4\zeta}{\beta E_0} \cot \theta. \quad (\text{A16})$$

For the $0 \rightarrow \pm 1$ transition, the corresponding ratio is:

$$r_{\pm 1} \equiv \frac{R_{\pm 1}^{[1]}}{R_{\pm 1}^{[2]}} = \frac{4E_{dc}}{E_0} - \frac{4\zeta}{\beta E_0} \tan \theta. \quad (\text{A17})$$

We now derive expressions for r_0 and $r_{\pm 1}$ in the presence of apparatus imperfections. In this case the fields \vec{E} , \vec{B} and $\vec{\mathcal{E}}$ are expressed as:

$$\vec{E} = (E_{dc} + E_0 \cos \omega t) \hat{x} + (e_y + e_y^r \cos \omega t) \hat{y} + (e_z + e_z^r \cos \omega t) \hat{z}, \quad (\text{A18})$$

$$\vec{B} = (b_x + f_B b_x^r) \hat{x} + (b_y + f_B b_y^r) \hat{y} + (b_z + f_B B_z) \hat{z}, \quad (\text{A19})$$

$$\vec{\mathcal{E}} = \mathcal{E}(\sin \theta \hat{y} + \cos \theta e^{i\phi} \hat{z}). \quad (\text{A20})$$

We include in this analysis the contribution of the M1 amplitude (eq. A4). The various terms in (A18, A19, A20) were introduced in section II. The presence of the small $b'_x = b_x + f_B b_x^r$ and $b'_y = b_y + f_B b_y^r$ components, in addition to the leading field $B'_z = b_z + f_B B_z$, is responsible for Zeeman mixing of adjacent m' sublevels of the 3D_1 state, which needs to be considered in deriving the expressions for the transition rate $R_{m'}$ and the harmonics ratios $r_{m'}$. One approach is to compute this mixing and modify the amplitudes of (A1, A2 and A3) accordingly. Alternatively, the fields \vec{E} , \vec{B} and $\vec{\mathcal{E}}$ can be rotated by application of an operator $\mathcal{D} = D(-a_y, \hat{y})D(a_x, \hat{x})$, such that $\mathcal{D}\vec{B} \propto \hat{z}$ [35]. The rotation angles are $a_{x(y)} = b'_{y(x)}/B'_z$. The rotated fields $\mathcal{D}\vec{E}$, $\mathcal{D}\vec{B}$, $\mathcal{D}\hat{k}$ and $\mathcal{D}\vec{\mathcal{E}}$ are used to evaluate the transition amplitudes of eqns (A1, A2 and A3). A great number of terms appear then in the expression for the rates $R_{m'}$. The corresponding harmonics ratios $r_{m'}$ are expanded in terms of the small field imperfections, the parameter κ and ζ . The ratios r_0 and $r_{\pm 1}$, retaining terms up to 2nd order in the expansion, are as follows:

$$r_0(\theta, f_B) = \frac{4E_{dc}}{E_0} - \frac{4(b_x + f_B b_x^r)e_z}{f_B B_z E_0} + \left[\frac{4\zeta}{\beta E_0} + \frac{4(b_x + f_B b_x^r)e_y}{f_B B_z E_0} \right] \cot \theta \cos \phi + \frac{4(b_y + f_B b_y^r)\zeta}{f_B B_z E_0} (1 + \cot^2 \theta \cos 2\phi), \quad (\text{A21})$$

$$r_{\pm 1}(\theta, f_B) = \frac{4E_{dc}}{E_0} + \frac{4e_y^r e_y}{E_0^2} \pm \frac{4e_y^r M 1 \kappa}{\beta E_0^2} + \frac{4(b_y + f_B b_y^r)\zeta}{f_B B_z \beta E_0} + \left[-\frac{4\zeta}{\beta E_0} - \frac{4(b_x + f_B b_x^r)e_y}{f_B B_z E_0} - \frac{4e_y^r e_z}{E_0^2} - \frac{4e_z^r e_y}{E_0^2} \mp \frac{4e_z^r M 1 \kappa}{\beta E_0^2} \right] \times \tan \theta \cos \phi \pm \frac{4e_z}{E_0} \tan \theta \sin \phi + \left[\frac{4(b_x + f_B b_x^r)e_z}{f_B B_z E_0} + \frac{4e_z^r e_z}{E_0^2} + \frac{4b_y \zeta}{f_B B_z E_0} \right] \tan^2 \theta \cos 2\phi \quad (\text{A22})$$

To compare the sensitivity of ζ/β measurements, made in different transition components, to false-PV effects, we form the combination K_1 [see eq. (13) and Table I] with use of r_0 and the sum $(1/2)(r_{-1} + r_{+1})$:

$$K_1^0 = \left[\frac{8\zeta}{\beta E_0} + \frac{8b_x^r e_y}{B_z E_0} \right] (\cot \theta_+ \cos \phi_+ - \cot \theta_- \cos \phi_-), \quad (\text{A23})$$

$$K_1^{\pm 1} = \left[-\frac{8\zeta}{\beta E_0} - \frac{8b_x^r e_y}{B_z E_0} - \frac{8e_y^r e_z}{E_0^2} - \frac{8e_z^r e_y}{E_0^2} \right] \times (\tan \theta_+ \cos \phi_+ - \tan \theta_- \cos \phi_-). \quad (\text{A24})$$

We see that there are more false-PV terms in $K_1^{\pm 1}$, compared to K_1^0 . A misalignment such that $e_y^r/E_0 = 0.005$, for instance, coupling to a stray $e_z = 50$ mV/cm, gives rise to a PV-mimicking signal of 0.25 mV/cm, which is $\approx 1\%$ of the measured PV effect. This is the primary reason why the isotopic comparison data were taken at the $0 \rightarrow 0$ transition component.

In section IV A 2 we discussed the measurement of the polarization ellipticity-related angle ϕ . This angle is determined by combining measurements of the difference $r_{+1} - r_{-1}$, made for opposite polarities of an enhanced e_z field ($\pm e_z$). Use of (A22) in this case yields:

$$(r_{+1} - r_{-1})_{+e_z} - (r_{+1} - r_{-1})_{-e_z} = \frac{16e_z}{E_0} \tan \theta \sin \phi \quad (\text{A25})$$

This expression was used in the analysis presented in section IV A 2.

Appendix B: Measuring θ_{\pm} using the 408 nm profile

Here we describe the method to measure the polarization angles θ_{\pm} using recorded profiles of the 408 nm resonance. These measurements are correlated with the concurrent readings of a polarimeter monitoring the light transmitted through the PBC, whose subsequent readings during a PV run are used to provide continuous tracking of the θ_{\pm} angles.

The polarization angles input to the PBC are set to approximately $\pm\pi/4$ (i.e. to the nominal values for which PV data are acquired) and are determined through analysis of the relative peak heights for the three transition components $m = 0 \rightarrow m' = 0, \pm 1$. Let $R_0^{[2]'}$, $R_{\pm 1}^{[2]'}$ be the 2^{nd} harmonic amplitudes of the $0 \rightarrow 0$ and $0 \rightarrow \pm 1$ transitions, given by:

$$R_0^{[2]'} = R_0^{[2]} + h(R_{-1}^{[2]} + R_{+1}^{[2]}), \quad (B1)$$

$$R_{\pm 1}^{[2]'} = R_{\pm 1}^{[2]} + hR_0^{[2]}, \quad (B2)$$

where $R_{m'}^{[2]}$ is the amplitude of the m' transition component in the absence of peak overlap, and $h = 0.00042(4)$ [introduced in (21)] is a parameter quantifying the slight overlap of adjacent peaks in the spectrum. The amplitudes $R_{m'}^{[2]}$ include a small correction for the slight saturation of the corresponding transitions (see section IV A 1). We form the quantity:

$$L(\theta, f_B; x_i) = \frac{1}{2} \frac{R_0^{[2]'} - R_{-1}^{[2]'} - R_{+1}^{[2]'}}{R_0^{[2]'} + R_{-1}^{[2]'} + R_{+1}^{[2]'}}. \quad (B3)$$

This parameter is a function of θ , the magnetic field flipping parameter f_B , and all apparatus imperfections (i.e. field imperfections and h), which we label as x_i . When $x_i \rightarrow 0$ then $L(\theta, f_B) = -(1/2) \cos 2\theta$, and $L = 0$ for $\theta = \pm\pi/4$. We adjust the input to the PBC polarization angles for an $L \approx 0$ reading (to within $1 \cdot 10^{-3}$), and use the measured values of L to determine the actual θ_+ and θ_- angles. For a given angle, we average measurements

made for both polarities of the magnetic field ($f_B = \pm 1$):

$$\bar{L}_{\pm} = \frac{1}{2} [L(\theta_{\pm}, f_B = +1; x_i) + L(\theta_{\pm}, f_B = -1; x_i)]. \quad (B4)$$

We use an approximate formula to relate \bar{L}_{\pm} to θ_{\pm} , that is derived by series expansion of (B4) in the small parameters x_i , and in θ_{\pm} around $\pm\pi/4$, respectively:

$$\bar{L}_{\pm} \approx (\pm\theta_{\pm} - \frac{\pi}{4}) \mp \frac{b_y^r}{B_z} - \frac{h}{4}. \quad (B5)$$

The θ_{\pm} angles corresponding to measured \bar{L}_{\pm} values are given by:

$$\theta_{\pm} \approx \pm \frac{\pi}{4} \pm \bar{L}_{\pm} + \frac{b_y^r}{B_z} \pm \frac{h}{4}. \quad (B6)$$

We see from (B6) that θ_{\pm} can only be determined with an offset b_y^r/B_z (estimated to be as large as a few parts per 10^3), which we do not have an accurate way to measure in the current apparatus [we do make a correction to θ_{\pm} to account for the contribution of the parameter h present in (B6)]. This offset, however, does not affect the determination of the parameter p_{θ} (18), used to calibrate the PV data. To show this, we expand $p_{\theta} = \cot \theta_+ - \cot \theta_-$ around $\theta_+ = \pi/4$ and $\theta_- = -\pi/4$:

$$p_{\theta} \approx 2(1 + \frac{\pi}{2} - \theta_+ + \theta_-), \quad (B7)$$

or, with use of (B6):

$$p_{\theta} \approx 2(1 - \bar{L}_+ - \bar{L}_- - \frac{h}{2}). \quad (B8)$$

We see that p_{θ} is independent of the imperfection b_y^r/B_z .